Observation of the Cosmic Ray Shadows of the Moon and the Sun Using the MINOS Far Detector

A paper describing the undergraduate research performed while pursuing the degree of Bachelor's of Science in Physics.

Samuel James Fogarty

Advised By: Dr. Alec Habig

Department of Physics and Astronomy
University of Minnesota Duluth
United States
Submitted to the University Digital Conservancy on December 13, 2019

Observation of the Cosmic Ray Shadows of the Moon and the Sun Using the MINOS Far Detector

Samuel James Fogarty

Abstract

Cosmic rays are high energy particles, mostly protons and helium nuclei, that create muons on collision with the atmosphere. The Moon and the Sun block cosmic rays in their travels, so there should be less muons seen in the directions of the Moon and the Sun. These effects are known as the 'cosmic ray shadows'. The purpose of this research was to find the cosmic ray shadows of the Moon and the Sun using muons observed by the MINOS Far Detector in the Soudan Mine in Soudan, MN. Muons deflect a considerable amount in the atmosphere and rock before they arrive at the detector, so there is a significant smearing effect in the shadows. This smearing effect makes resolving the shadows difficult, so a shadow template was created using Monte-Carlo methods. The template represents what the shadows should actually look like with muon deflection in mind. A background was created (using a Monte-Carlo method) to be the Null hypothesis that represents what the muon data would look like if the Moon and the Sun were not present. The shadow template, background, and signal histograms were compared using a Log-Likelihood Analysis to produce cosmic ray shadows of the Moon and the Sun seen by the Far Detector. The Moon and Sun shadows were produced using 141 million cosmic ray muons observed from October 2003 to September 2016. Confirming the expectation, the Moon shadow was shown to not vary much over time, whereas the Sun shadow varied considerably over time and was much less significant. The statistical nature of cosmic ray muon deflection was explored using binomial statistics and Monte-Carlo methods. It was shown that single and double cosmic ray muon deflection can be simulated using binomial statistics and Monte-Carlo methods.

Contents

1 Chapter 1: Introduction, Background, and Motivation

1.1 Introduction

1.1.1 Neutrinos and Cosmic Rays

Neutrino detectors have been active around the world for decades. They have the ability to observe the interactions of neutrinos with matter. Neutrinos move at close to the speed of light, have very little mass, have a neutral charge, and they interact with other particles via the weak force. Their use of the weak force makes them very weakly interacting, so they often can travel through the entire Earth without interacting with anything. This makes detecting neutrinos incredibly difficult. But, on occasion, a very unlucky neutrino will interact with an atom and produce more particles which can be seen by neutrino detectors. Those new particles are more massive and charged compared to the incident neutrino, commonly electrons, muons, and taus. Since neutrino detectors can see charged particles from neutrino interactions, if those same particles happen to originate from another source, such as cosmic ray air showers, the detectors will see them too. This makes some neutrino detectors great at detecting muons from cosmic rays. These muons are the subject of this research.

Neutrinos come in three flavors: electron, muon, and tau neutrinos. Each flavor produces a different charged lepton upon interacting with matter. An electron neutrino produces an electron, a muon neutrino produces a muon, and a tau neutrino produces a tau. The observation of one of these particles after a neutrino interaction can help to indicate the type of neutrino that interacted in the first place. For example, observing a muon tells you that the interacted neutrino may have been a muon neutrino, and the same goes for electrons and taus. Not all neutrino detectors can observe all three neutrino interactions.

Since detectors of neutrinos are designed to be able to detect electrons, muons, and/or taus, it is often a common occurrence that they see those particles from other sources besides neutrinos. A cosmic ray (CR) is made primarily of protons and some helium nuclei, but all stable nuclei up to Uranium have been found in varying amounts [1]. When they collide with the atmosphere at high altitudes they produce cosmic ray air showers. An air shower is generated when a single high energy primary CR nucleus or photon hits the upper atmosphere [2]. (A "secondary" cosmic ray is generally an anti-proton produced when a primary cosmic ray collides with an atomic nucleus in the interstellar medium [2].) π and K mesons are produced in the air shower cascade which decay into muons. A muon has a charge of ± 1 and has a much larger mass than the electron. Muons from CR air showers are often detected by neutrino detectors because they penetrate a long way through matter. For example, and as it is relevant to this research, the MINOS Near and Far Detectors were capable of seeing these muons from cosmic rays. The "cosmic ray muons" seen by

the Far Detector were the subject of this research.

1.1.2 Cosmic Ray Shadows

The goal of this research has been to create histograms demonstrating the CR shadows of the Moon and the Sun. The Moon and the Sun are such large and massive objects that they block all CRs coming from behind them. Thus there is an expected deficit ("shadow") of CRs from their directions. Of course, a deficit of CR muons should be directly indicative of a deficit of CRs, so there is an expected deficit of muons to be seen in the directions of the Moon and the Sun in the sky. However, there are a few problems that make that less of a 1:1 comparison, such as the non-uniformity of the CR muon flux over the sky and CR muon scattering in the rock overburden. These will be described in detail in later sections. Cosmic ray shadows have been observed by numerous detectors around the world including but not limited to the MINOS Far Detector in Soudan, MN [3], Tibet-III AS Array in Tibet, China [4], IceCube at the South Pole [5], and the MACRO Detector in Gran Sasso, Italy [6]. This paper will describe how the CR shadows of the Moon and Sun were produced and will explore the statistical nature of CR muon scattering.

1.2 Why Cosmic Ray Shadows?

1.2.1 Solar Magnetic Field Influence on Cosmic Rays

It is important to talk about why finding CR shadows is a useful and worthwhile endeavor. The hadronic parents of CR muons are repeatedly pushed around in their journey through space to the detector. This push is a result of magnetic fields that permeate space, where the force due to the Lorentz force is proportional to the charge and the cross product of the velocity and magnetic field. The solar wind carries charged particles, mainly ionized hydrogen and helium, outward from the Sun and through space which generates the heliospheric magnetic field as a result of their movement [7]. The area where the solar wind has its largest influence is called the heliosphere. While a CR traverses through the heliosphere, its trajectory is continuously altered. The solar wind is subject to variations depending on solar activity, so the heliospheric magnetic field varies over the approximately 11 year solar cycle. Since the field varies, so does the total influence it has on CR trajectories. There is also an analogous interstellar wind that produces an interstellar magnetic field in the galaxy, but this is irrelevant for this research.

1.2.2 Geomagnetic Field Influence on Cosmic Rays

The effect of Earth's magnetic field may also have an impact on CRs. If it were assumed that there was no atmosphere on Earth, the question of whether a CR will reach the surface is dependent on only the

magnitude and direction of the local magnetic field and the rigidity and direction of the charged particle's movement [7]. Rigidity is the measure of the momentum of a charged particle in units of momentum per charge. The higher the rigidity of a particle, the more it can resist deflection by magnetic fields. If one equates the centripetal force and the Lorentz force (assuming negligible electric field), this yields the equation of $r = \frac{m\vec{v}^2}{q\vec{v}\times\vec{B}}$, where r is the radius of curvature, m is the mass of the particle, $\vec{v}$ is the velocity of the particle, q is the charge, and $\vec{B}$ is the magnetic field strength. This equation says that the greater the particle velocity, the greater the radius of curvature and thus less deflection (and smaller velocity yields more deflection). Also, the greater the magnetic field is, the more deflection occurs. If someone were interested in studying and observing this phenomenon [8] then it would be smart to target the Moon shadow over the Sun shadow. The Sun shadow would be too influenced by the heliospheric magnetic field for any geomagnetic field effects to be easily observable. The Moon shadow is expected to be minimally influenced by the heliospheric magnetic field, so geomagnetic fields would be more easily observable using Moon shadows. The geomagnetic effect has not been explored in this research, but it may still be present in the data and Moon shadows nonetheless. For example, it is possible that the center of the Moon shadow can be shifted west, as found by Amenomori et al. [8].

1.2.3 The Effect on the Moon and Sun Shadows

These effects can be large enough that the apparent trajectory of a CR at Earth is not the same as its true trajectory it had as it passed the Sun. In this research, how much CRs were deflected while outside the solar system was not considered. More specifically, only how much a CR was deflected as it passed the Moon or the Sun on a path towards the Earth was considered. This is because variations from the expected shadows were sought. The expected shadows are what the shadows would look like right after the CRs either passed the Moon or the Sun or were absorbed by one of them. In this research, the shadow expectations were altered to include the CR muon scattering effect which will be explained in detail in a later section. In a period of strong heliospheric magnetic field strength, CRs coming from the Sun's distance heading Earthward will be deflected a large amount thanks to the large distance that they have to travel and the strong magnetic field strength. It is possible that the appearance of the Sun shadow may vary quite considerably over the period of a solar cycle. More variations from the expectation in the Sun shadow are expected near a solar maximum (high field strength), and fewer variations are expected near a solar minimum (low field strength). This variability has been experimentally shown by the Tibet Air Shower Array [9]. The Moon, on the other hand, is 400 times closer to the Earth than the Sun, so there is much less distance over which CRs can deflect from the heliospheric magnetic field. As a result, it is expected that the Moon shadow should not vary as considerably over time as the Sun shadow should.

The geomagnetic field varies over time but much more slowly than the heliospheric magnetic field [7]. Although both effects are time dependent, the heliospheric effect will likely be the main observed effect in a month to month or year to year solar shadow analysis. The effect of the solar magnetic field on the Sun shadow and the lack of its effect on the Moon shadow outlines one of the uses for CR shadows. Sun shadows can be used to study the solar magnetic field variability over time [9], and Moon shadows can be used to study the geomagnetic field [8]. In this research, only shadows for the full 13 year period of the MINOS Far Detector muon data set were made. Nevertheless, the influence of the solar magnetic field on the Sun shadows was observed.

1.2.4 Using Shadows for Detector Resolution and Pointing

Thanks to the greater time dependence of the heliospheric effect, many more variations are expected from the expectation in the Sun shadow than the Moon shadow. As such, the Moon shadow is a great way to determine detector stability and resolution. This is because Moon shadows should not vary much over months and years. Moon shadows have been used in the past for this very purpose, even for the MINOS Far Detector [3]. It is known with very high precision where the Moon has been in the sky and its size when a muon was detected. As a result, it is known exactly what a CR shadow of the Moon should look like. Any variations from that expectation are indications of the limited angular resolution of a detector. This angular resolution includes the multiple Coulomb scattering effect of muons unless the effect is accounted for. The angular resolution of a detector refers to its ability to accurately reconstruct particle trajectories. Besides the structural factors that contribute to a detector's angular resolution, CR muon scattering in the rock overburden above the detector is a natural factor that contributes to it as well. A problem arises when the angular resolution of a detector is greater than approximately 0.25°. This is approximately the angular radius of the Moon and Sun in the sky. A large enough angular resolution could make resolving CR shadows more difficult. When the CR muon scattering contribution is on average greater than 0.25°, the effect will likely have an impact on the shadows. See in Figure 9, where the number of muons seen within the Moon is non-zero as a result of CR muon deflection. This happens when a CR muon, coming from a primary CR that had just missed the Moon or the Sun, scatters in the rock overburden to essentially "fill up" the shadow to some extent. This could spell trouble for resolving CR shadows. In this research, CR muon scattering was simulated using a Monte-Carlo method to create Moon and Sun shadow expectation histograms. Those histograms represent what the shadows were expected to look like with the muon scattering effect in mind.

Any variations from the shadow expectation for the Moon could help indicate detector problems. Thus Moon shadows are a very useful tool in neutrino detector diagnostics. It may be of interest to use the

muons seen by a detector to find specific CR sources. This requires as large of an angular resolution as possible in order for this kind of research to be successful. This also requires high pointing reliability. This is because a star, unlike the Moon and the Sun, takes up a small portion of the sky. They thus would have a relatively small effect on CR flux compared to the Moon and the Sun, or at least an effect relegated to a smaller region of the sky. In order to accurately examine a precisely chosen (and small) region of the sky, the detector in question must be able to reliably reconstruct particle trajectories. For instance, if the center of a Moon shadow, where the histogram is centered at the Moon, was in a place other than the very center (where it is expected to be), this would indicate bad pointing reliability for the detector. The search for CR sources is only one example of something on which bad pointing would have a negative impact. Bad pointing has an impact on all research avenues that require accurate particle trajectory reconstructions. This underlines how useful Moon shadows can be.

1.2.5 The Prominence of the Geomagnetic Effect

The geomagnetic field effect was not investigated in this research. This is because it is not expected that the effect would be prominent using the MINOS Far Detector. There are two reasons why the geomagnetic field effect would not be observed. For one, the CR muons seen by the MINOS Far Detector must have been somewhat high energy muons. Intensity of muons decreases with increased depth underground (but eventually flattens out at further depths) [2]. This means that muons would have had a considerably high velocity to have enough energy to make it through the 705 m of rock to the detector. Thus lower energy muons will generally not make it to the detector, and thus only the higher energy muons would remain. Those high energy muons must also have come from high energy CRs. As it was explained, high momentum particles are less deflected by the geomagnetic field as compared to lower momentum particles. Hence any possible effect due to the geomagnetic field observed in a CR muons analysis would likely be minimal for the Far Detector. The Near Detector, on the other hand, has a larger range of muon energies as a result of it being closer to the surface. It is more likely that the effect will be observable in Near Detector Moon shadows. The second reason why the geomagnetic effect would not be prominent is that at the Far Detector's latitude, according to the Stormer Cutoff Rigidity function [7], the effect is small. The function shows that the cutoff rigidity for a CR entering the atmosphere depends on the zenith angle considered. It is lowest at 45° west, then higher at 0°, and highest at 45° east. The cutoff rigidity is how much rigidity (momentum per charge) a particle requires to enter the atmosphere. The magnitude of this effect depends on the geomagnetic latitude so, at the Far Detector's geomagnetic latitude, the effect is small.

1.3 Personal Growth

I have been working on this research project since May 2018. I am thankful for the opportunity UROP has provided me to further my research during the summer of 2019. In the beginning of my research, I was very reliant on the help of my supervisor. Over time, I realized that I have the ability to solve most of my research problems on my own. It is the realization of this ability that has allowed me to grow as a researcher, where I have gained the ability to be independent in research. I have also learned research techniques and skills that I can utilize in future coursework, future research, and in graduate school. This research has also been a great coding experience. My coding abilities have grown and flourished and my understanding of programming languages has deepened thanks to my research experience.

2 Chapter 2: The MINOS Far Detector

2.1 The Fermilab Neutrino Oscillation Experiments

The MINOS Far Detector is part of Fermilab's project to probe the physics of neutrino oscillations. Fermilab's neutrino oscillation project is mostly made up of three main components: The NuMI (Neutrinos at the Main Injector) neutrino beam in Batavia, Illinois pointed North, a "Near Detector" that observes neutrino interactions 1 km downstream from the neutrino production target, and a "Far Detector" that records neutrino interactions at a much further distance away. The Far Detector and Near Detector will be referring to as "FD" and "ND" respectively from now on. Both detectors measure the beam's flavor composition and energy spectrum. A detector is built so far away from the beam to give the neutrinos time to oscillate to other flavors. The Main Injector Neutrino Oscillation Search (MINOS) experiment was a long baseline neutrino oscillation experiment made up of a ND and a FD. The FD was located in the Soudan Underground Laboratory in Soudan, MN, 735 km away from the MINOS ND (located at Fermilab) [10]. MINOS was eventually shut down and replaced by the larger NuMI Off-Axis Neutrino Appearance (NOvA) experiment, where the NOvA Far Detector was built in Ash River, MN. The NOvA experiment is still running in 2019 and will be eventually succeeded by the Deep Underground Neutrino Experiment (DUNE) to be built in Lead, South Dakota. The Near Detectors were/are exposed to a very high flux of neutrinos due to their proximity to the beam, but the Far Detectors, at their distance from the beam, observe(d) much fewer neutrinos. This meant that the Far Detectors had to be built much larger than the Near Detectors. The immense sizes of these detectors is required due to the minuscule neutrino-nucleon cross section for producing a charged lepton. The cross section is on the order of 10^{-38} cm^2. A flux of about 1 neutrino per $cm^{-2}s^{-1}$ (1 GeV neutrinos) leads to an expected average of about 100 neutrino interactions per kiloton per year [2]. This case shows how rarely neutrinos interact with nucleons. It explains why detectors are required to be so large. The MINOS FD was 705 m underground, so most of the CR muons at the surface were blocked by the rock overburden as they traversed to the detector. The FD only saw on the order of 0.5 Hz of CR muon events [11].

2.2 MINOS Far Detector Composition

The 5.4 kT MINOS FD was 705 m underground and was composed of 486 octagonal planes with a single 1.5 m air gap between the two super-modules. The first super-module had 249 planes (14.78 m in length) and the second had 237 planes (14.10 m in length). There was a 2.41 cm air gap between each plane for mechanical reasons. Each plane consisted of a 2.54 cm thick layer of steel and a layer of 4 cm wide by 1 cm

thick plastic scintillator strips [10]. The steel provided a relatively inexpensive target for neutrino interactions and about 95 % of the bulk mass of the detectors. The strips were at most the length of a plane (8 m) and the plane is filled with these strips side by side (arranged in eight separate modules on each plane). There are 192 strips on each plane with the exception of the first and last planes. Every plane's layer of scintillator alternates direction to get a 3-dimensional image of the incoming particles. The scintillator strips point 45 ° from the vertical. See Figure 1.

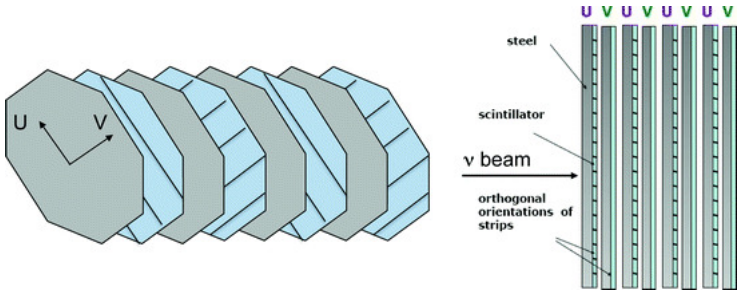

Figure 1: **Schematic of the MINOS FD showing the alternating steel and scintillator planes (steel first, scintillator second, and so on). Every scintillator plane has strips perpendicular to the previous scintillator plane. "U" and "V" represent the two strip orientations. Figure originally from Ochoa [10].**

2.3 Far Detector Magnetic Field

Unlike the newer NOvA detectors, the MINOS detectors have magnetic fields. Each super-module has its own magnetic coil which toroidally magnetizes the steel layers to an average field strength of 1.42 T in the FD. The magnetic coils of the ND and the FD were designed and optimized separately as a result of the available infrastructures available at both Fermilab and Soudan, so there are some differences between the two, although, the fields in both detectors were required to have similar strengths to minimize systematic uncertainties [11]. There are two main purposes for the magnetic field in the MINOS detectors. The first purpose is to differentiate between muon neutrinos and muon anti-neutrinos by measuring the curvature of muons and anti-muons. The second purpose is to estimate the momentum of muons by measuring their curvature.

2.4 Atmospheric Neutrino-Induced Muons and Veto Shields

The MINOS detectors could also observe atmospheric neutrino interactions. Atmospheric neutrinos are products of the decay of particles including pions and kaons in CR air showers [2]. If one of these neutrinos is muon flavored and interacts inside the detector, it will be registered as a muon neutrino just like the muon neutrinos from the NuMI beam. These muons would begin inside the detector fiducial volume

(the volume of the detector where events are accepted, typically smaller than the total volume) instead of on the boundary like a typical CR muon. It is also possible that a CR muon would travel through the air gaps between two planes and then interact inside the fiducial volume, therefore mimicking an atmospheric neutrino interaction.

Three Veto Shields were installed in the FD for the purpose of differentiating between atmospheric neutrino-induced muons and beam muons (see Figure 3). There is one above and one on either side of the detector. The one above is made of two layers of scintillator and the sides have one layer each, where each has no layer of steel present [12]. This allows for CR muons, that sneak in through the air gaps, to be seen entering the detector. Thanks to the Veto Shields, it is known whether a muon was an atmospheric neutrino-induced muon or simply a sneaky CR muon. The Veto Shield configuration is repeated four times along the 30 m length of the FD to allow for full coverage with some overlap to eliminate cracks. The strips are also orientated to point North to South along detector length.

2.5 Scintillator Used in the Detectors

The scintillator is made of extruded polystyrene strips. Each has a groove through the middle on the surface that houses a fiber optic cable along the entire length of the strip. The fiber optics are wavelength-shifting (WLS) fibers that absorb blue (near ultraviolet) light (420 nm) and re-emits it as green light (530 nm) which is transported via total internal reflection to an optical connector and then a photo-multiplier tube to record the signal [11]. The strips have a layer of titanium oxide to contain the scintillation light (it will reflect inside until it is absorbed by the WLS fiber) and a reflective seal that covers the top of the strips. See Figure 2. A polystyrene molecule absorbs energy from the Coulomb interaction between it and a charged particle passing by. The molecule transitions to an excited state and, in less than a nanosecond, de-excites to its ground state releasing energy in the form of a near ultraviolet photon. The purpose of the WLS fiber is to absorb this photon and re-emit it as a lower energy photon (green) that is transported to the optical connector. This helps to ensure that the scintillation light does not get reabsorbed then re-emitted repeatedly by other scintillator molecules.

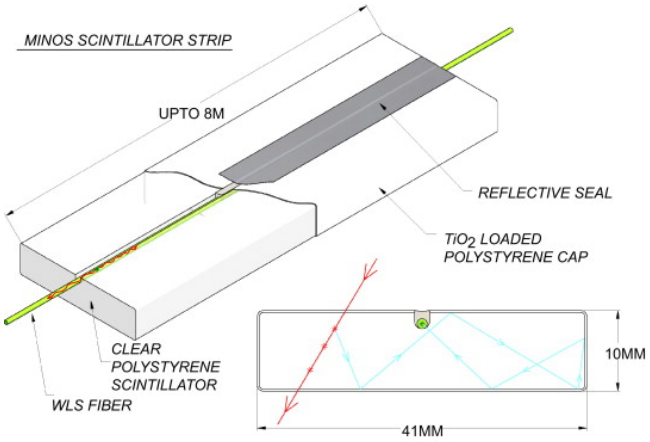

Figure 2: **A scintillator strip is up to 8 m long and has a Wavelength Shifting fiber down the middle covered by a reflective seal. Strips are painted white with Titanium Oxide. Figure originally from D. G. Michael et al. [11].**

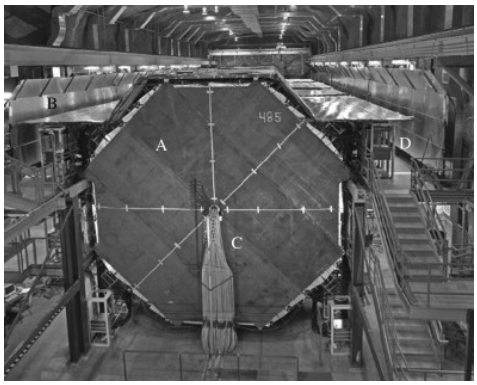

Figure 3: **The MINOS Far Detector in Soudan, MN. The Far Detector Veto Shields can be seen on the top of the detector. Figure originally from D. G. Michael et al.** [11]

3 Chapter 3: Data Set, Cuts, and the Background

3.1 Required Steps for Making Shadows

There are three main histograms that need to be created to prepare for the Log-Likelihood analysis in Section 4. The first is a two-dimensional histogram of the muon data sample centered at the Moon/Sun. This is a distribution of muon events seen in the sky by the FD in coordinates of right ascension and declination. The second is a two-dimensional histogram of the background present in the muon sample. This will be the Null hypothesis for the shadows. The Null hypothesis is defined to be what the muon sample would look like if the Moon or the Sun were not present. This is important for the Log-Likelihood analysis that considers the likelihood that the shadow could be explained by random oscillations in the background. The background will be determined using Monte-Carlo simulation. The third is a two-dimensional histogram that represents the expected shape of the shadow. This is necessary because CR muon scattering in the rock overburden causes a significant smearing effect in the shadows. This histogram will be the template of what the Moon and Sun shadows are expected to look like with muon scattering. It is with these three histograms that the Log-Likelihood binned analysis will be performed to produce CR shadows of the Moon and Sun.

3.2 Moon and Sun Ephemera

It is important that the histograms are centered at the Moon or the Sun. In order to center them, it must be known where the Moon or the Sun were at the time of each muon detection. A C++ script was created that takes Local Sidereal Time (LST) and Julian Date (JD) of a muon as inputs. It outputs the position and angular size of the Moon and the Sun. The formulas used are from Practical Astronomy with Your Calculator by Duffett-Smith [13]. The angular sizes of the Moon and the Sun were also calculated using this book. To the calculations, corrections for parallax of the Moon and nutation of the Earth were added (for the Moon and the Sun). Nutation is an effect of the Sun and the Moon tugging on the non-spherical Earth causing its rotation axis to gyrate slowly with a period of about 25800 years [13]. The correction is on the order of 10 or less arc seconds. The correction may not be a necessary correction for finding the shadow. Parallax is the effect where an object appears to be in slightly different positions depending upon the observer's position. The effect is negligible for the Sun because of its great distance from the Earth, but it is very evident for the Moon. In retrospect, it may not be necessary to calculate the size of the Sun at each moment for the shadows since it does not vary much over time. Although this was not investigated this further, it may be a potential short cut for finding the Sun shadows.

3.3 Data Set and Cuts

3.3.1 Celestial Coordinates

The data set used in this analysis is 14.09×10^7 CR muons seen by the MINOS Far Detector from October 2003 to September 2016. The frequency of muons seen by the FD depends on zenith and azimuth angles. Zenith and azimuth are called horizon coordinates because they refer to the plane of an observer's horizon. Azimuth is measured from the direction north (direction of the geographic north pole as opposed to the magnetic north pole) 360° around and zenith is measured from the point directly over an observer's head to the horizon (0 to 90 °) [13]. Other coordinates used are the set of astronomical coordinates called right ascension and declination. Right ascension is measured Eastward in hours (0 - 24 h) on the celestial sphere from the Vernal Equinox all the way around. The Vernal Equinox is defined to be the position of the Sun on the first day of Spring seen at the equator, so this point changes every year. Declination is measured Northward along the celestial sphere from the celestial equator (0 - 360 °) [13].

3.3.2 Zenith and Azimuth Effects on Muon Flux

In Figure 8, the zenith and azimuth effects on observed muons can be seen for the FD. The only cuts to the data made for those histograms were a restriction to only using single track muons and muons with starting interaction vertices at the detector edges. Nearly all of the interaction vertices land on the edges of the detector (this indicates where muons entered the detector). Only single track muons are used to make CR shadows, but double track muons will be utilized as well. Double muon events are where a primary CR is energetic enough to produce two muons instead of one. Interaction vertices that occur outside the detector come from badly reconstructed muon tracks and thus are not useful for my analysis and are cut. Figure 4 demonstrates this cut for the FD.

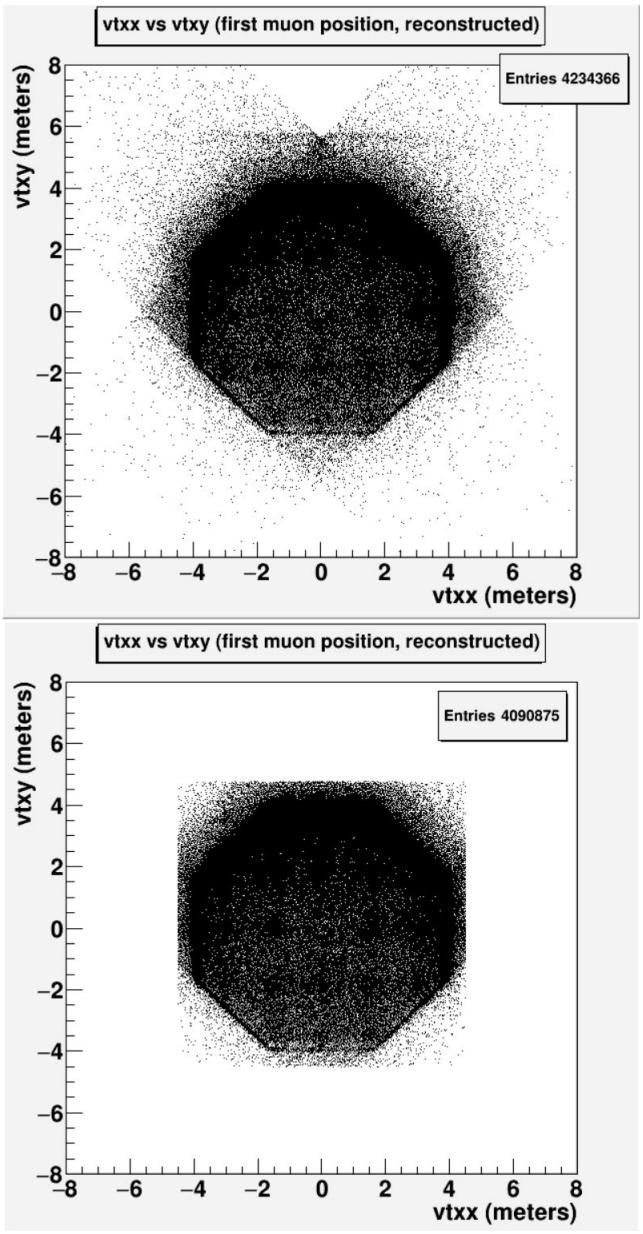

Figure 4: **Initial interaction vertices of cosmic ray muons seen by the MINOS Far Detector in the $x - y$ plane without vertex cuts (top) (z-axis out of the page). Initial interaction vertices with vertex cuts on the bottom. Notice the many muon vertices that appear outside the detector edges which are a result of badly reconstructed muon trajectories. The octagonal shape of the detector can be clearly seen.**

3.3.3 Rock Overburden and Zenith Cut

Notice that the number of muons seen in Figure 8 increases with increasing zenith angle (towards the horizon), reaches a peak around 35 °, then slowly drops until about 80 °. The drop to zero is a result of the depth of the FD. Angles at 80 ° or more constitute significant rock overburden for incoming muons. This

introduces the first data cut: to not use muons seen at angles greater than 80 °. It is very unlikely that a CR muon will make it through all the rock overburden at 80 ° or more, so any muons seen at those angles are necessarily not CR muons. Muons at these angles would need to be produced by neutrinos that interact somewhere in the Earth to produce a muon (*i.e.* an atmospheric neutrino from an air shower). These muons do not constitute CR muons so they are cut from the analysis.

3.3.4 Geometric and Atmospheric Depth Effects on Muon Flux

What explains the other striking trend in the zenith histograms? The increase from 0 to approximately 35-40 ° and eventual decrease is a result of the combination of geometric and atmospheric depth factors. As in Figure 5, a larger zenith angle θ corresponds to a larger solid angle.

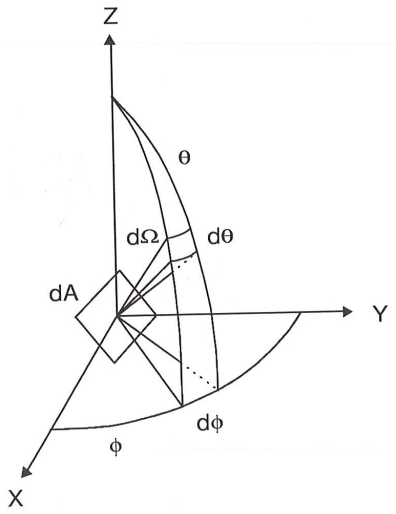

Figure 5: **This figure shows one octant of a sphere. $d\theta$ is an infinitesimal element of zenith angle, $d\phi$ is the infinitesimal element of azimuth angle, and $d\Omega$ is the infinitesimal solid angle. A larger θ produces a larger $d\Omega$ as a result of the geometry. A greater solid angle means there is a larger region available for CRs to interact with atmosphere, thus leading to the effect of increasing muon frequency. Plot taken from Grieder [7].**

Notice how the solid angle $d\Omega$ goes to zero at $\theta = 0°$. This can be seen using equation 1 [7]:

$$d\Omega = sin(\theta)d\theta d\phi \tag{1}$$

The greater solid angle provides a greater region for CRs to interact with. Thus more muons at larger zenith angles than at lower zenith angles are expected (assuming CRs are uniformly distributed in space). However, this is not completely what is seen in Figure 8. There is a *decreasing* trend for muon frequency at $\theta >\sim 35°$. This is due to a competing effect of zenith angle dependence of muon frequency due to at-

mospheric depth. Looking at equation 2, $I(0°)$ is the intensity at $\theta = 0°$ and n_i is a very large number depending on the composition of the atmosphere (approximately $2.687 * 10^{19}$ for air) [7].

$$I(\theta) = I(0°)cos^{n_i}(\theta) \tag{2}$$

At $\theta = 0°$, the intensity $\theta = 0°$ is found. And at $\theta = 90°$, the intensity becomes 0. $I(\theta)$ decreases from $\theta = 0°$ to $\theta = 90°$ because of the properties of cosine. According to this, it sounds like there should be less muons at greater zenith angles. This is confirmed by Figure 6, where the intensity of muons observed should decrease with increasing atmospheric depth. Atmospheric depth (atmospheric thickness) also increases with increasing zenith angle (see Figure 7). There are two competing effects here, where it seems that the switch between dominance due to either effect happens at the peak, *i.e.* $\sim 35°$.

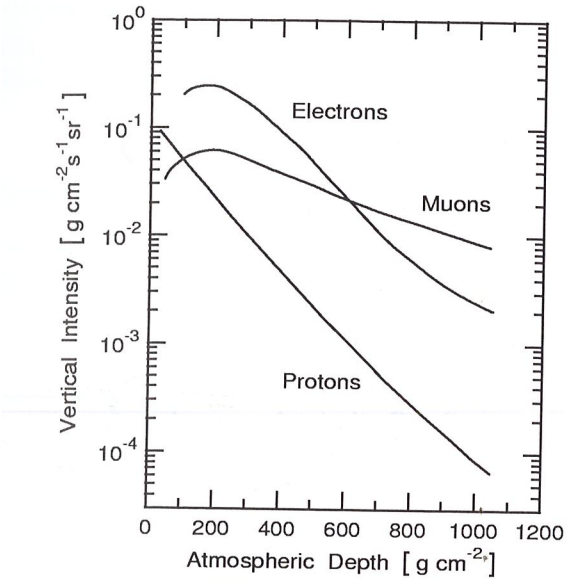

Figure 6: **Depth of the atmosphere and intensity of muons are directly related. An increase in atmospheric depth leads to the general trend of a linear decrease of intensity on a log scale, that is, after a slight increase at low atmospheric depth. Plot taken from Grieder [7].**

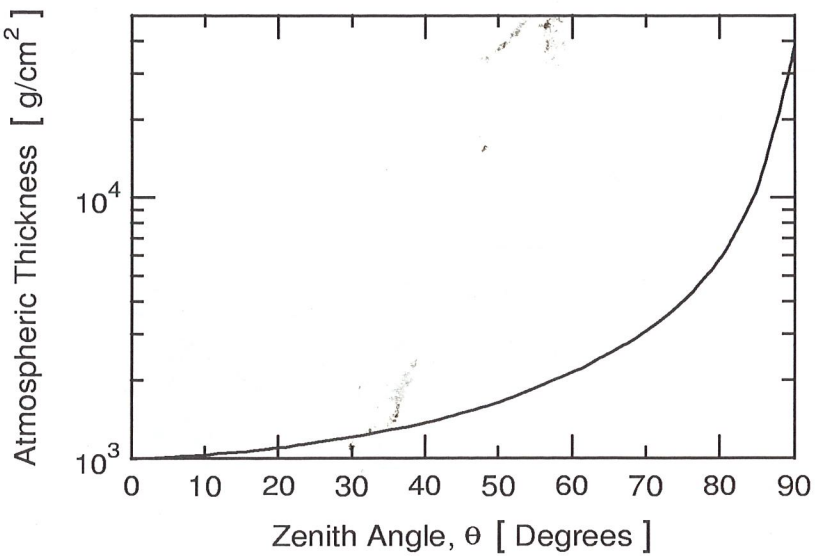

Figure 7: **This figure shows the zenith angle θ dependence on atmospheric thickness (*i.e.* depth). There is the largest thickness of atmosphere at the horizon and lowest at $\theta = 0°$. Plot taken from Grieder [7].**

3.3.5 Plane and Track Length Cuts

Referring to Figure 8, the azimuth histograms show the trend of the frequency dropping to nearly zero close to 60 ° and 250 °. This is a result of the structure of the detector. The detector was made up of vertically oriented planes, such that muons coming in on the sides of the detector were more likely to miss every plane and pass through unnoticed. Muons seen in these areas on the histograms are likely to have passed through relatively few planes. A track that passes through few planes will not be reconstructed reliably. This introduces the next cut. Only muons that pass through greater than or equal to 9 planes are used in this analysis. This cut comes from a similar CR shadow analysis for the FD [3]. Another cut applied is restricting tracks to only be greater than 1.55 m in length. This is because a shorter track length will not be reliably reconstructed [3]. All cuts made to the data are tabulated in Tables 1 and 2.

Cut	No. Remaining	Fraction Remaining
Before Any Cuts	16.62×10^7	100%
Number of Tracks = 1	16.11×10^7	96.92%
Number of Planes ≥ 9	14.52×10^7	87.36 %
Track Length $\geq 1.55\,\mathrm{m}$	14.14×10^7	85.05 %
Zenith Angle $\leq 80.0\,^\circ$	14.11×10^7	84.90 %
$-4.5 < vtx_x < 4.5, -4.5 < vtx_y < 4.75$	14.09×10^7	84.79 %

Table 1: **This table shows the cuts made to the whole data set of cosmic ray muons seen by the Far Detector from October 2003 to September 2016.**

Cut	No. Remaining	Fraction Remaining
Total Double Muons	42.04×10^5	100%
Number of Planes ≥ 9	41.28×10^5	98.21 %
Track Length $\geq 1.55\,\mathrm{m}$	39.92×10^5	94.96 %
Zenith Angle $\leq 80.0\,^\circ$	39.83×10^5	94.74 %
$-4.5 < vtx_x < 4.5, -4.5 < vtx_y < 4.75$	39.21×10^5	93.28 %

Table 2: **This table shows the cuts made to the data set of cosmic ray double muons seen by the MINOS Far Detector from October 2003 to September 2016.**

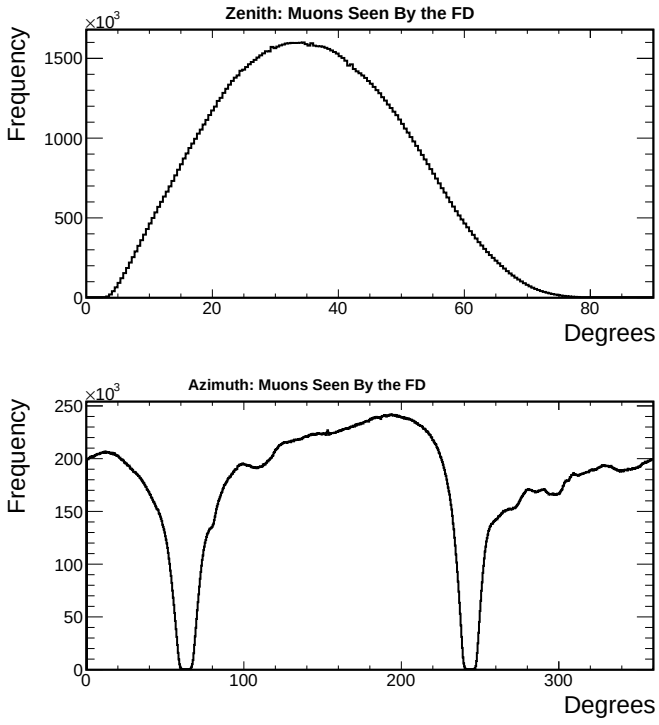

Figure 8: **Number of muons seen by the MINOS Far Detector over zenith (top) and azimuth (bottom) angles from October 2003 and September 2016.**

3.3.6 Data Set Organization

The data set is organized into runs and subruns. A run consists of typically no longer than 24 hours of data taking. A subrun consists of 1 hour chunks of data taking. Each run is made up of many subruns. This organization puts the data into "bite sized pieces" to be easier to work with. For instance, organizing data into hour sized chunks allows for specific subruns to be cut from the data set if necessary. For instance, if the detector was having problems for a short period of time, the data taken during that time was typically not saved.

3.4 Data Analysis Tools

ROOT is the tool used in this analysis [14]. ROOT was developed by CERN and is designed for big data processing, statistical analysis, and visualization and storage of data. The abilities of ROOT that are most utilized in this research is the system of "Trees" and 1D and 2D histograms for visualization of data. The TTree class has a hierarchy of branches that make data access easy and computationally fast. Along with ROOT, C++ is used in this analysis.

3.5 1D and 2D Deficits of Muons Around the Moon and Sun

The first step to finding CR shadows is to look for the 1D CR shadows. It is expected that these 1D shadows will demonstrate the muon deficit at the Moon and the Sun. To do this, it was calculated where the Moon and Sun were at the time of each muon detection (Section 3.2). The angular position of each muon in celestial coordinates (right ascension and declination) is already known, so now the difference between the angles was found. This difference represents the one-dimensional angular distance $\Delta\theta$ each muon is from the Moon or the Sun at the time of detection. This represents a shift in the coordinate system. In Figure 8, the zenith angles represent the angular distance a muon is from the zenith ($\theta = 0°$). In the 1D deficit histogram, the angles now represent the angular distance a muon is from the Moon or the Sun instead of the zenith. In order for the shadowing effect to be visible in the 1D deficit histograms, the geometric effect present in the zenith distribution in Figure 8 must be accounted for in the form of a normalizing factor. This normalizing factor was applied as a weight for each muon's $\Delta\theta$ before it was filled into the histogram. The factor is an inverse solid angle

$$N = \frac{1}{\pi(r_2^2 - r_1^2)} \tag{3}$$

where $r_2 = \Delta\theta + b$, $r_1 = \Delta\theta$, and b is the bin size for the histogram. The solid angle used to find N

is approximately true for small $\Delta\theta$. This works for the range of angles used in Figure 9. After applying the normalizing factor, the histograms in Figure 9 were found. These histograms demonstrate the actual muon frequency around the Moon and Sun, albeit in units of deg^{-2}. In both histograms, there is a clear decrease in frequency while approaching zero and a flat region at larger angles. The decrease in frequency confirms that there is a shadowing effect caused by the Moon and the Sun. The flat regions show that the range of the shadowing effect is limited to a small region around both the Moon and the Sun. Figure 9 also demonstrates that the deficit does not go to zero at the center of the Moon or the Sun. This result is expected because of the CR muon scattering that occurs in the rock overburden. This represents a preliminary step which demonstrates that the shadowing effects can be observed. It also demonstrates that muon scattering has a significant impact on the apparent shadowing effect. Thus the effect will need to be accounted for to produce two-dimensional CR shadows.

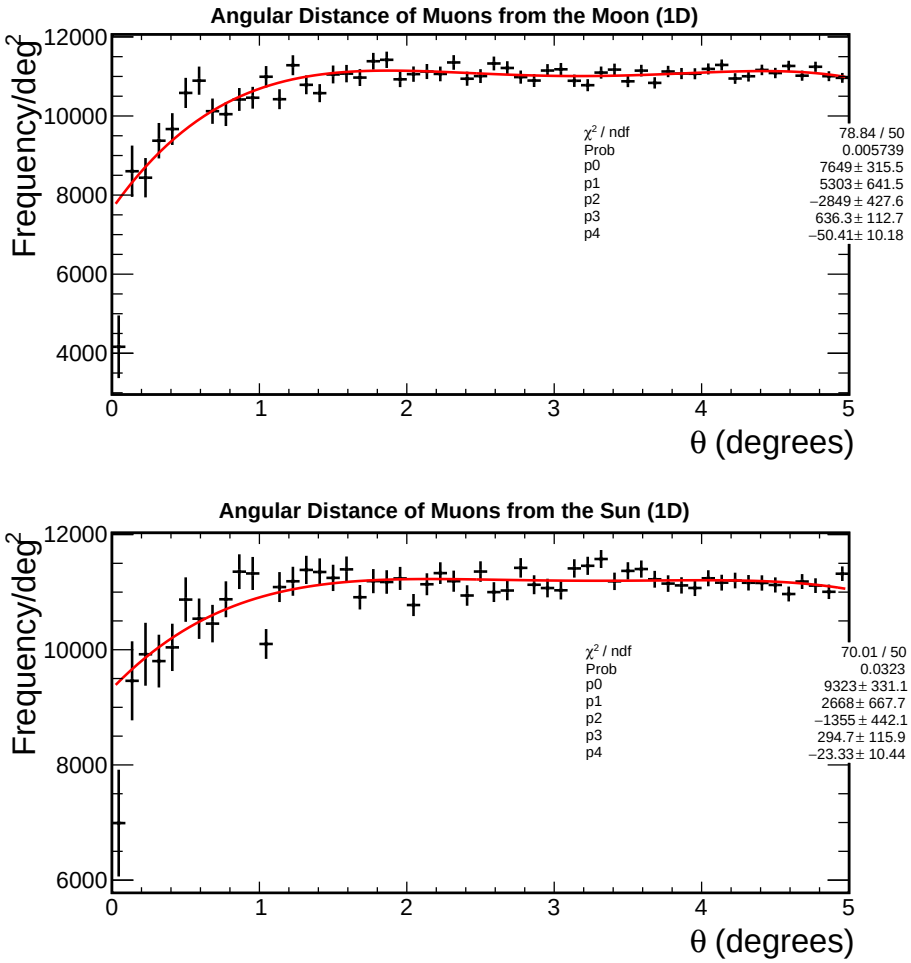

Figure 9: **Apparent 1D muon deficits (in units of deg^{-2}) seen in the regions around the Moon and Sun by the MINOS Far Detector.** 0° **is the center of the Moon/Sun. Fit using a built-in ROOT fourth-order polynomial function. Data used was from October 2003 to September 2016.**

The next step is to produce 2D histograms similar to the 1D deficit histograms in Figure 9. This time around, no normalizing factor was added to tame the geometric effect. The Log-Likelihood analysis to be performed utilizes a simulation of the data set that 1) does not contain Moon and Sun shadowing effects and 2) simulates all other geometric and physical effects (*i.e.* atmospheric depth, rock overburden, *etc*). As a result, the geometric effect will eventually be taken care of by the Log-Likelihood analysis in Section 4. The 2D histograms to be created represent the "signal" present in the sample. The signal represents the CR muons seen in the regions within and surrounding the Moon or the Sun in the presence of shadowing effects. It was found by taking the difference ΔRA and ΔDEC between the position of the Moon or the Sun and the position of a muon in right ascension and declination (Figure 10). Figure 10 has no obvious shadowing effects present, unlike Figure 9. This is only because no normalizing factor was

used. The 2D signal histogram in Figure 10 is the first component completed (out of three) required to create CR shadows. What is left to do now is to produce a simulated background and a simulation of the Moon/Sun shadow expectation.

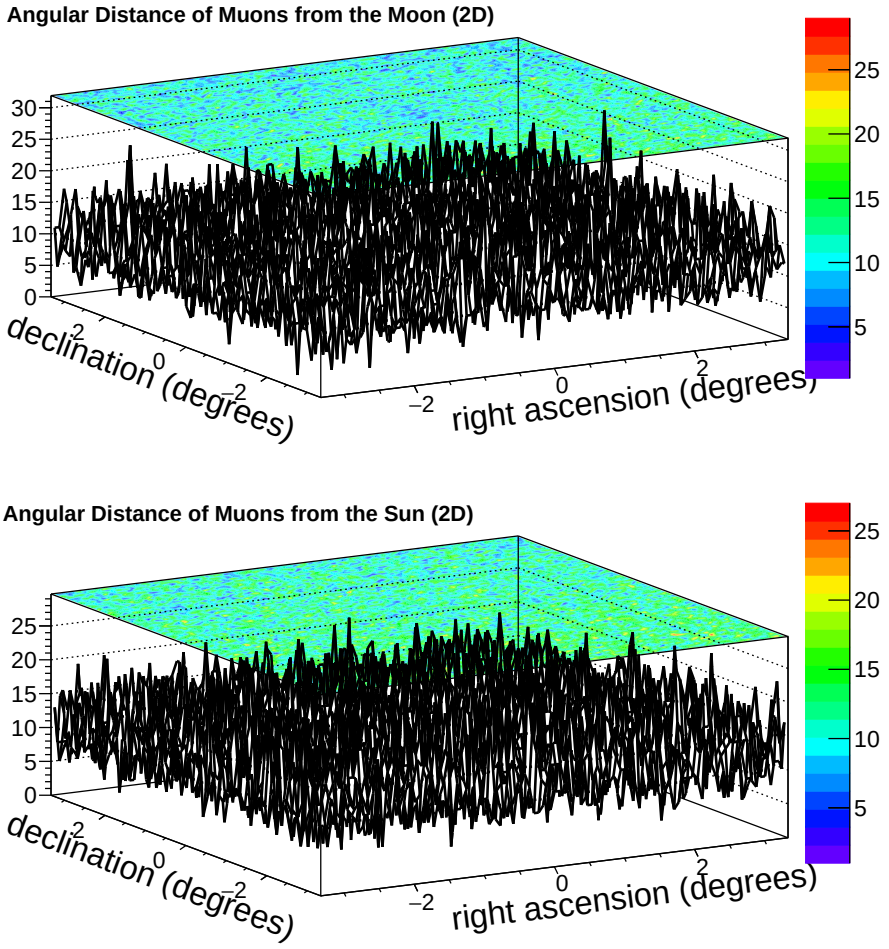

Figure 10: **Apparent frequency of muons observed around the Moon and the Sun by the MINOS Far Detector in right ascension and declination. No normalizing factor was used here to tame the geometric effect, so the deficits are especially hard to see in this form. Data used was from October 2003 to September 2016.**

3.6 Cosmic Ray Muon Scattering

As noted previously, muons deflect as they travel through the atmosphere and rock overburden to the detector. This effect can be quantified by focusing on the case of double muons. By creating a histogram of double muon separation angles, that histogram can be converted into one of single muon deflection angles. Double muons occur when one high energy CR collides with the atmosphere to produce two approximately

parallel muons. Double muons have very small initial separation angles [6], such that it can be assumed that the original separation angle of each pair was 0°. As the pair of muons travels toward the detector, the two particles will deflect from their original trajectories. When they are detected, they will have a new separation angle.

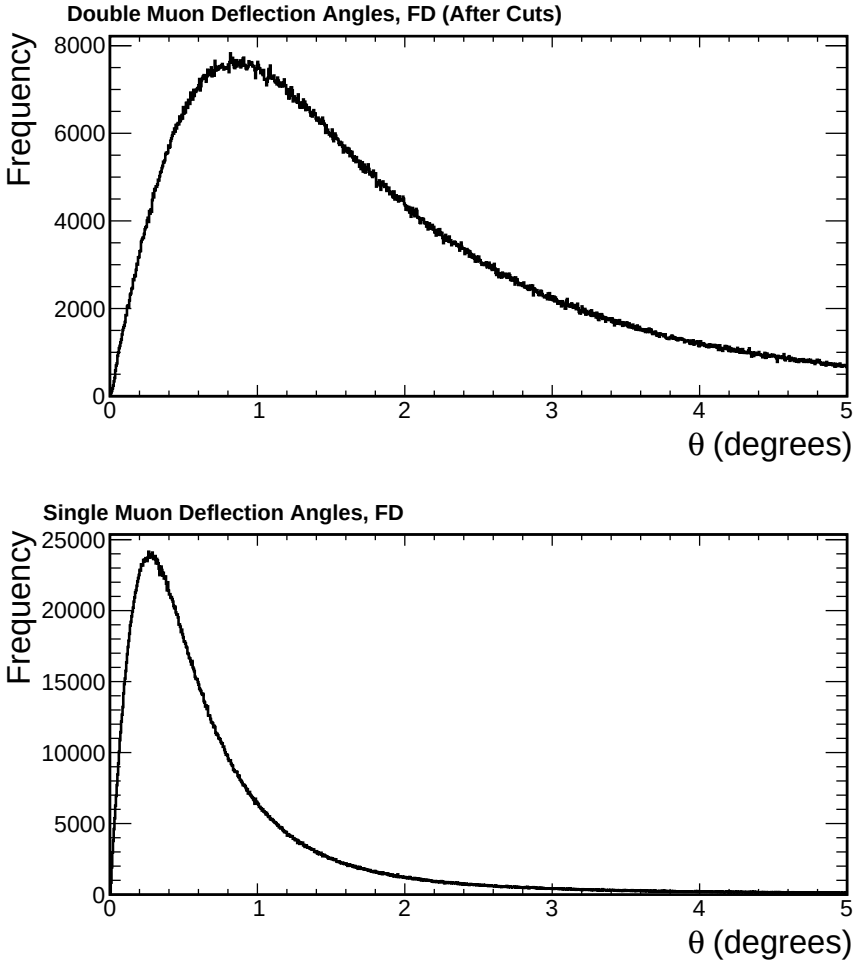

Figure 11: **Angles between double muons (top) and single muon scattering angles (bottom) in the MINOS Far Detector (with data cuts from Table 2 applied). Data used from September 2003 to October 2016. Cuts included: Planes, track length, interaction vertices.**

This can be quantified by finding the angle between the two muons' direction cosine unit vectors. In Figure 11, the distribution of double muon separation angles for the FD is shown (using the cuts outlined in Table 2). This distribution can be converted to single muon deflection angles by dividing each angle by the $\sqrt{2}$ because each muon takes a different path during the deflection process. The single muon deflection angles for the FD are demonstrated in Figure 11. The angles decrease slightly as a result of the inclusion of the $\sqrt{2}$ factor. This histogram can be used as an estimate of how much any single muon deflects from its

original trajectory. This distribution will be used to form the expected shapes of the Moon and Sun shadows. This factor of $\sqrt{2}$ will not be used without some proof. In the next section, evidence of this factor will be shown. It will demonstrate the incredible statistical nature of the CR muon scattering and simulate the single and double muon scattering distributions with Monte Carlo methods.

3.7 Galton Board Simulation

3.7.1 Galton Board

The Galton Board, named after English scientist Sir Francis Galton, is a device that performs many statistical experiments. It is made of a board with a triangular array of evenly spaced pegs arranged in staggered order similar to Pascal's Triangle. Tiny beads are let fall through a small funnel onto the top peg where they are allowed to either move left or right. After they move on from the first peg, they will encounter another peg where they can go left or right, and so on until the bottom. The board is restricted to a single plane, so the only two possible directions are left and right. At the bottom is a row of evenly spaced rectangular slots to hold the fallen beads. In an idealized Galton Board, neglecting the elasticity of the beads and other factors, the beads have a probability of moving left of 0.5 and a probability of going right of 0.5. Letting the Galton Board run produces a Gaussian (Normal) distribution in the rectangular slots. It may not be obvious, but this device works under the same principle as muon deflection. First there will be a description of how the Galton Board was simulated, then the problem will be expanded into three dimensions to simulate the single and double muon deflection distributions.

3.7.2 Galton Board Simulation Procedure

To start, a loop over the total number of beads n to drop is done. Beads will be simply referred to as "particles" from now on. These particles, like in the Galton Board, start at the same "peg" when they begin their descent, but, the pegs do not need to be physically simulated in this simulation. This is taken care of by setting a number N that represents the number of steps, *i.e.* the total number of pegs a particle will hit before it reaches the bottom. (It is important to assume in this simulation that each particle never misses a peg during its descent.) A random number generator is used that generates either a 0 or a 1, each with a 50% chance of occurring. Each particle starts at $x = 0$, where x represents the position along the x-axis (bottom of the board). If a 0 is generated, 1 is subtracted from x. If a 1 is generated, a 1 is added to x. (This is one "Left-Right" trial.) Each addition or subtraction represents a movement of left or right at each peg by 1 unit. Turns out, it won't matter in the end what exactly a "unit" is; so, it will continue to be arbitrary. This step, of either moving left or right, is repeated until N steps have elapsed. n trials

are performed; one trial for each particle. To review what has happened thus far, this procedure drops n particles and performs N Left-Right trials on each bead. The distribution produced by this series of trials and experiments should form some form of binomial distribution. This is because a binomial distribution is produced by a series of Bernoulli trials like in this problem. Figure 12 shows the result of many Galton trials, where it appears identical to the real life Galton Board.

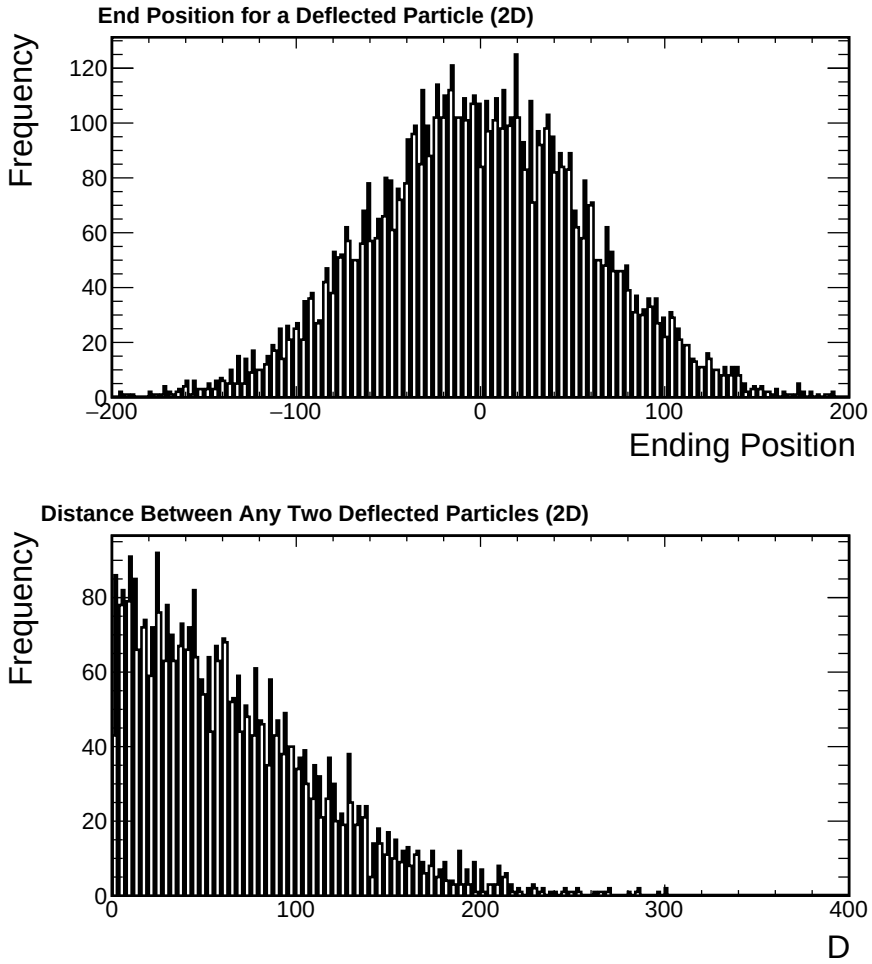

Figure 12: **Galton Board simulation using binomial probabilities, where the x-axis represents the final position of a particle along the x-axis (top). Distance between any two fallen particles along the x-axis (bottom).**

Figure 12 has a distribution of distances between sets of two beads. There are half as many entries in the histogram since this "distance between" operation halves the number of entries. Both histograms are analogous, somewhat naïvely at this stage, to the single and double muon deflection distributions. The purpose of this investigation is to see if there is a similar process happening for CR muons, but it is clear the 2D Galton Board does not describe it. The next step (after a small detour) is to expand this simulation to

three-dimensions.

3.7.3 Finding the Average Value for the Galton Board

It is perhaps not all too surprising that the mean of a Galton Board (Figure 12) would be at $x = 0$, especially if the beads start at $x = 0$. It is also not surprising that the Galton Board produces a Gaussian distribution, since binomial probabilities can be approximated with a Gaussian distribution. One can find the mean of this distribution analytically starting with the equation for binomial probabilities, namely

$$b(X, n, p) = \binom{n}{X} p^X (q)^{n-X} \tag{4}$$

where n is the total number of Left-Right trials and p and q are the probabilities of the two outcomes. In the Galton Board problem $p = q = 0.5$, so this simplifies to

$$b(X, n) = \binom{n}{X} \frac{1}{2^n} \tag{5}$$

and expanding the combination yields

$$b(X, n) = \frac{n!}{(n - X)!X!} \frac{1}{2^n} \tag{6}$$

X is often referred to the number of "successes" given n trials. A success will be defined as the number of times the particle moves right, denoted by R. This slightly modifies equation 6 into

$$b(R, n) = \frac{n!}{(n - R)!R!} \frac{1}{2^n} \tag{7}$$

Equation 8 describes the probability of getting R rights given n steps. R is currently unknown. The goal is to get R in terms of knowns, such as x and n (those are generally specified). Recall that x is the position along the x-axis, so it can be expressed as a combination of rights R and lefts L (exploiting the fact that rights and lefts move the particle by 1 unit) such that

$$x = R - L \tag{8}$$

x is defined to be the following for any n:

$$x = -n, -n + 2, -n + 4, ..., n - 4, n - 2, n \tag{9}$$

Similarly, as in Equation 8, the number of trials can be expressed as a combination of R and L too, with

$$n = R + L \tag{10}$$

where again, R and L are the total number of rights and lefts respectively that the particle moves in one Galton trial. Equations 8 and 10 represent two equations with two unknowns, so R and L can be solved for in terms of x and n.

Solving these two equations yields

$$L = \frac{n - x}{2} \tag{11}$$

$$R = \frac{x + n}{2} \tag{12}$$

Equations 11 and 12 say something profound about the Galton Board. If n is fixed at some value but x can be any integer value, how many lefts and rights can a particle make to reach position x? What these equations suggest is that there is a unique combination of L and R that yield x. In other words, there is only one combination of lefts and rights that will move a particle into a position x. This does not necessarily mean that there is only one *path* to get to x. There could be more than 1 path, since the particle could go down many different paths while still performing the same number of lefts and rights. This may not seem surprising but it is an interesting result nonetheless.

If Equation 12 is plugged into to Equation 7, this yields

$$b(x, n) = \frac{n!}{(n - \frac{x+n}{2})!\frac{x+n}{2}!}\frac{1}{2^n} \tag{13}$$

Simplifying gets

$$b(x, n) = \frac{n!}{(\frac{n-x}{2})!(\frac{x+n}{2})!}\frac{1}{2^n} \tag{14}$$

Of course, the definition of the average value μ is

$$\mu = \sum_x x f(x) \tag{15}$$

where $f(x)$ is some probability distribution. Substituting Equation 14 into Equation 15 yields the following average value of x:

$$\mu = \sum_x x \frac{n!}{(\frac{n-x}{2})!(\frac{x+n}{2})!}\frac{1}{2^n} \tag{16}$$

If the summation is carried out using the definition of x from Equation 9 and simplified, Equation 16 be-

comes

$$\mu = \frac{n!}{2^n} \sum_{i=0}^{n} \frac{-n+2i}{i!} \frac{1}{(n-i)!} \tag{17}$$

It is expected that μ will end up equaling zero, so based on Equation 17 the only part that can be zero is

$$\sum_{i=0}^{n} \frac{-n+2i}{i!(n-i)!} \tag{18}$$

The goal now is to check if this expression equals zero or not. Expanding Equation 18 reveals that

$$\sum_{i=0}^{n} \frac{-n+2i}{i!(n-i)!} = \frac{-n}{n!} + \frac{-n+2}{(n-1)!1!} + \frac{-n+4}{(n-2)!2!} + ... + \frac{n-4}{(n-2)!2!} + \frac{n-2}{(n-1)!1!} + \frac{n}{n!} = 0 \tag{19}$$

Equation 19 equals zero because every term has an equal and opposite signed term on the other side of the summation, so they all cancel out. If Equation 19 equals 0, then it means that

$$\mu = 0 \tag{20}$$

This confirms the simulation nicely and shows that with more trials, the mean approaches 0. The purpose of this investigation of the mean is that it is a stepping stone to finding the mean for a three-dimensional Galton Board. A three-dimensional Galton Board actually turns out to be a very good simulation of CR muon scattering in the atmosphere and rock overburden. As such, finding the mean and standard deviation of the 3D case may provide valuable insight into CR muon scattering.

3.7.4 Three-Dimensional "Galton Board"

A Galton Board constrains particles to a single plane, only being able to move left, right, or down. This constraint does not apply to muons since they are able to move in three-dimensions. A muon, theoretically, has a infinite number of directions it can move. For instance, it can move left or right, forward or backward, at 45°, 225°, 32.3°, 245.3° and so on at any angle around a circle. So clearly, a more complex method is required to simulate this new problem. This new method is quite similar to the 2D case in that it works under the same principles. Let η be the number of possible directions in which a particle could move, n be the number of steps, and N be the number of trials (particles). In the 2D case, $\eta = 2$ where there are 2 possible directions in which to move. Clearly, one cannot perform a simulation where $\eta = \infty$, but the simulation can be approximated with a very large η. In the simulations coming up, $\eta = 10000$ was chosen. There are η possible directions each labeled from 0 to $\eta - 1$. Now a uniform random integer is generated between 0 and $\eta - 1$ which chooses the direction in which the particle will move during the current

step. This makes it so every direction has an equal probably of occurring. This last step is done for all n in the beginning before anything else, so it will already be known all the directions that the particle will move in and the number of times it moves in those directions before the next steps are performed. Those numbers are put into a histogram with an x-axis going from 0 to $\eta - 1$. The purpose of the histogram is to store how many times the particle moves in each direction to be used in the rest of the simulation.
Now a loop through the histogram bins is performed: The first bin represents the first direction counter-clockwise from the positive (right pointing) x-axis. The angle ϕ is the angle from the positive x-axis that a direction points. Each direction has a ϕ, but to convert to Cartesian coordinates each angle is adjusted to be within the first quadrant. Once it is in the first quadrant, the total displacement in that direction is converted to x and y displacements with basic trigonometry. Then to correct for the signs, ϕ is used to adjust the signs of x and y back to their correct quadrants. The x and y displacements for each direction (histogram bin) are added to the total displacement along the x and y axes. At the end of this loop, the final position of a particle has been found after it has gone through n steps along η possible directions. The steps in this paragraph are repeated N times (for each particle).

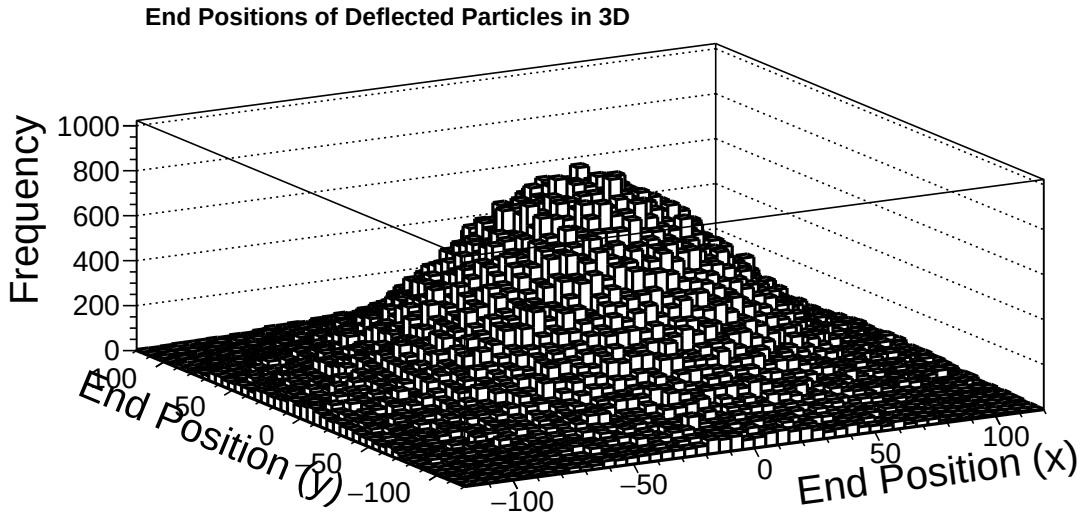

Figure 13: **Simulation of single particle deflection in 3D with $n = 5001$ steps, $\eta = 10000$ directions, and $N = 300000$ trials.**

Figure 13 is a histogram that shows how all the particles are distributed on the $x - y$ plane at the end of the simulation. Figure 14 has a histogram with distance from the origin d on the x-axis, where $d = \sqrt{x^2 + y^2}$. It represents how far a single particle is deflected in 3D space in dimensionless units. Also in Figure 14 is an identical histogram but with deflection angle θ on the x-axis. This angle is found by con-

sidering two vectors $\vec{u}$ and $\vec{v}$, where $\vec{u} = 0\hat{i} + 0\hat{j} + n\hat{k}$ and $\vec{v} = x\hat{i} + y\hat{j} + n\hat{k}$. The magnitudes are $||\vec{u}|| = \sqrt{0^2 + 0^2 + n^2} = n$ and $||\vec{v}|| = \sqrt{x^2 + y^2 + n^2}$. $\vec{u}$ is the vector that points along the z-axis and $\vec{v}$ is the vector that points from the starting position (same for all particles) to the ending position for a particle. θ is found by

$$\theta = cos^{-1}(\frac{\vec{u} \times \vec{v}}{||\vec{u}|| * ||\vec{v}||}) \tag{21}$$

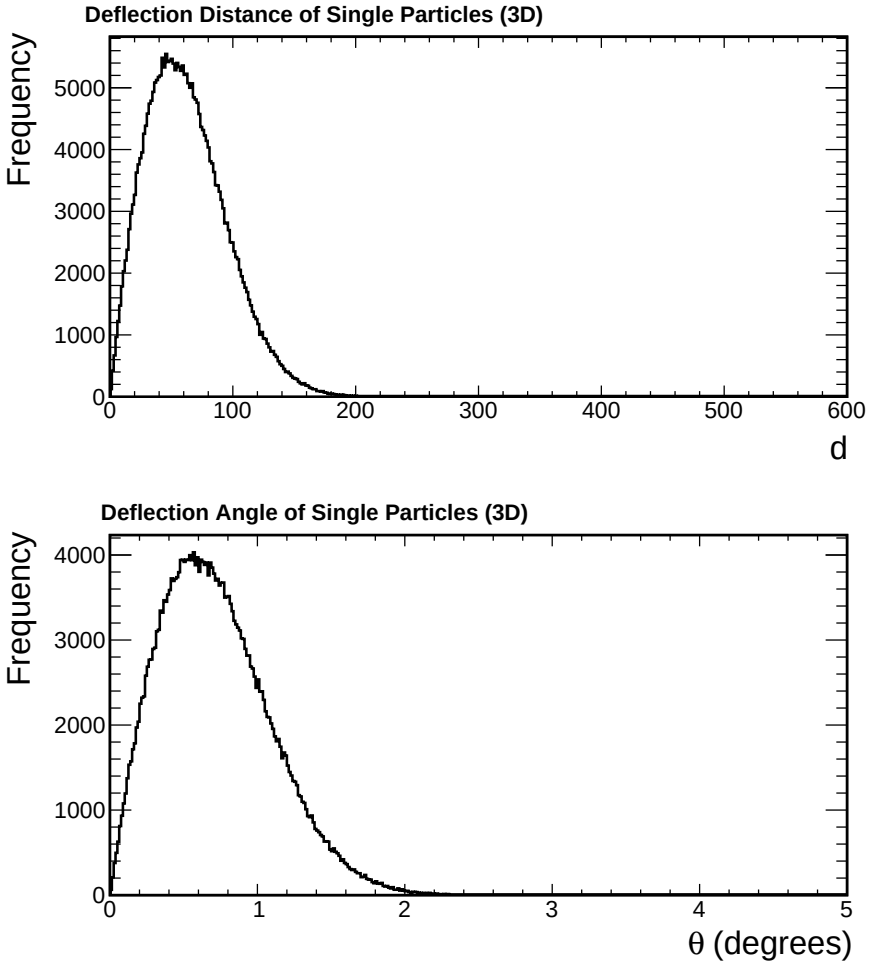

Figure 14: **Simulation of single particle deflection with $n = 5001$ steps, $\eta = 10000$ directions, and $N = 300000$ trials. Deflection distance d from the origin of single particle (top) and deflection angle θ of single particle from starting position (bottom). Notice that the bottom histogram looks remarkably similar to the single muon deflection angles seen by the Far Detector in Figure 11.**

Similarly the distance D and angle α between any two particles can be found. $D = \sqrt{(x_1 - x_2)^2 + (y_1 - y_2)^2}$, where x_1 and y_1 are the displacements of the first particle along the x and y axes respectively and x_2 and

y_2 are the displacements for the second particle. D is visualized in Figure 15. α is found in the same way that θ was found, but now where $\vec{u} = x_1\hat{i} + y_1\hat{j} + n\hat{k}$ and $\vec{v} = x_2\hat{i} + y_2\hat{j} + n\hat{k}$. The magnitudes are $||\vec{u}|| = \sqrt{x_1^2 + y_2^2 + n^2}$ and $||\vec{v}|| = \sqrt{x_2^2 + y_2^2 + n^2}$. Then α is found via Equation 21. The deflection angles between two particles are visualized in Figure 15.

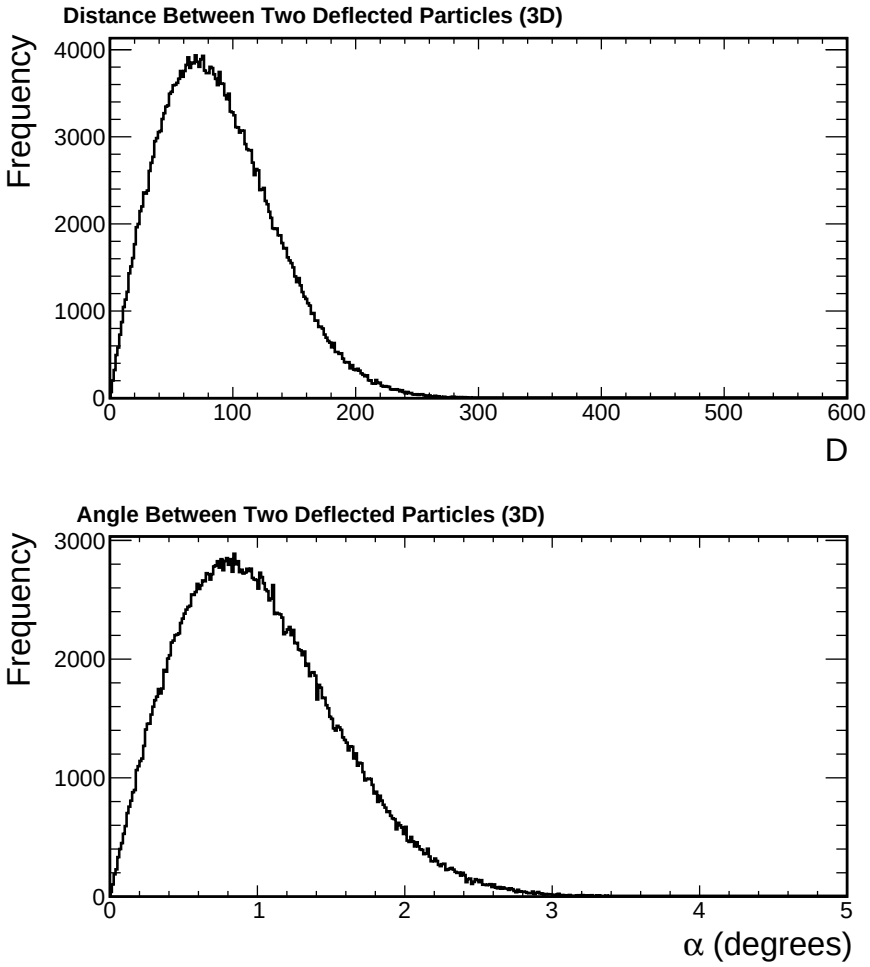

Figure 15: **Simulation of double particle deflection with $n = 5001$ steps, $\eta = 10000$ directions, and $N = 300000$ trials. There are 150000 entries because this is essentially 150000 two particle trials. Deflection distance D between two particles (top) and deflection angle α between two particles (bottom). Notice that the bottom histogram looks remarkably similar to the double muon deflection angles seen by the Far Detector in Figure 11.**

Figures 14 and 15 are the same types of distributions as the single and double muon deflection distributions seen by the FD in Figure 11. The $\sqrt{2}$ factor at this point should hopefully be hidden in these simulations somewhere. What can be done now is to take Figure 15 and divide each angle by $\sqrt{2}$ to make a new histogram of angles. This new histogram (Figure 16) should be identical to Figure 14. In Figure 16, this modified histogram is shown next to the histogram from Figure 14. The two distributions are almost

exactly identical in shape, mean, and standard deviation. The greater the number of trials N the closer these distributions converge to each other.

This procedure has demonstrated the $\sqrt{2}$ factor in a way that provides justification for using it in the shadow analysis. An assumption is being made that the physics of single and double muon deflection is dominated by binomial statistics, which are what the simulations are based off of. This assumption is likely correct because of the similarity between the shapes and x-axis angle ranges of both the simulated and FD distributions. It may be possible to find the factor analytically using binomial or multinomial statistics.

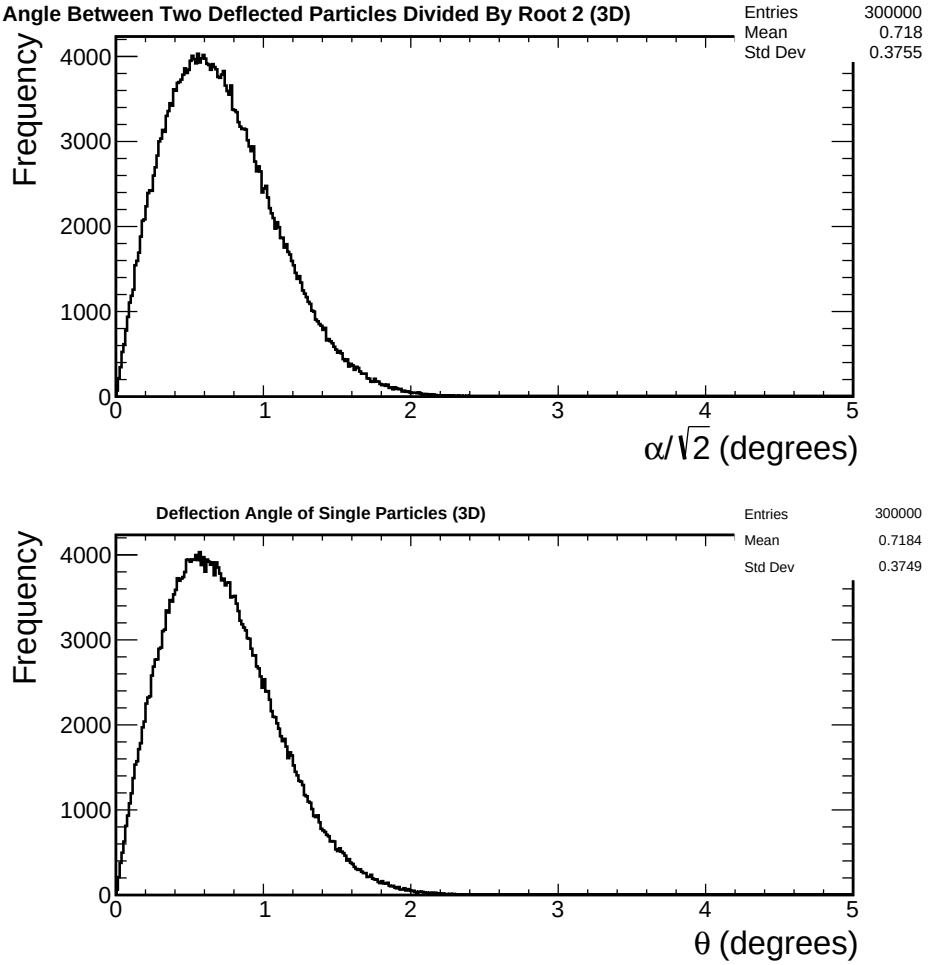

Figure 16: **Histogram of $\alpha/\sqrt{2}$ modified two-particle deflection angles and histogram of θ single-particle deflection angles from origin. The means (0.7180 and 0.7184) and standard deviations (0.3755 and 0.3749) are almost identical, where increasing the number of trials causes these numbers to approach the same values. This demonstrates that 'double particle' (double muon) deflection angles α can be converted to 'single particle' (single muon) deflection angles by dividing by $\sqrt{2}$.**

3.8 Shadow Templates

In Section 3.6, it was described how CR muons are deflected as they travel to the detector. This will create a smearing effect in the shadows. It is the goal of this section to create a shadow template histogram, using a Monte-Carlo method, that describes what the shadows are expected to look like with CR muon scattering. This template will be used in Section 4 in the Log-Likelihood analysis to find the CR shadows. To begin, random numbers need to be generated to represent x_0 and y_0 positions for a muon. x_0 and y_0 are the initial positions for a CR muon before it has deflected at all. To do this, a uniform random number is generated on a range from -10.0 to 10.0 for x_0 and separately again for y_0 on the same range. It is known that this muon will deflect a certain distance r at a certain angle β. These two values will need to be randomly generated or sampled for each 'simulated' muon. For β, a uniform random number is generated on the range from 0.0° to 360.0°. This determines the direction in which the simulated muon will deflect. For r, a random θ is sampled from the FD single muon deflection distribution (Figure 11). This determines the total angle over which the simulated muon will deflect. The final positions of a simulated muon will be $x_2 = x_1 + rcos(\beta)$ and $y_2 = y_1 + rsin(\beta)$. These final positions are all put into a 2D histogram that will be used to normalize the template from 0 to 1. The final positions are put into another 2D histogram (the unnormalized Moon/Sun template) *only* if x_0 and y_0 were outside the Moon or Sun radius (there should be no muons coming from the Moon or the Sun). This procedure of generating and deflecting a simulated muon is performed 120 times for each muon seen by the FD. This is equivalent to 120 times the amount of data collected by the FD. The Moon and Sun radii are found using the time and date of each muon [13]. The unnormalized template histogram is divided by the normalization histogram to create the normalized Moon and Sun templates (Figure 17). Figure 17 demonstrates how even if a CR misses the Moon (or the Sun), there is a chance that it will deflect and fill up the shadow.

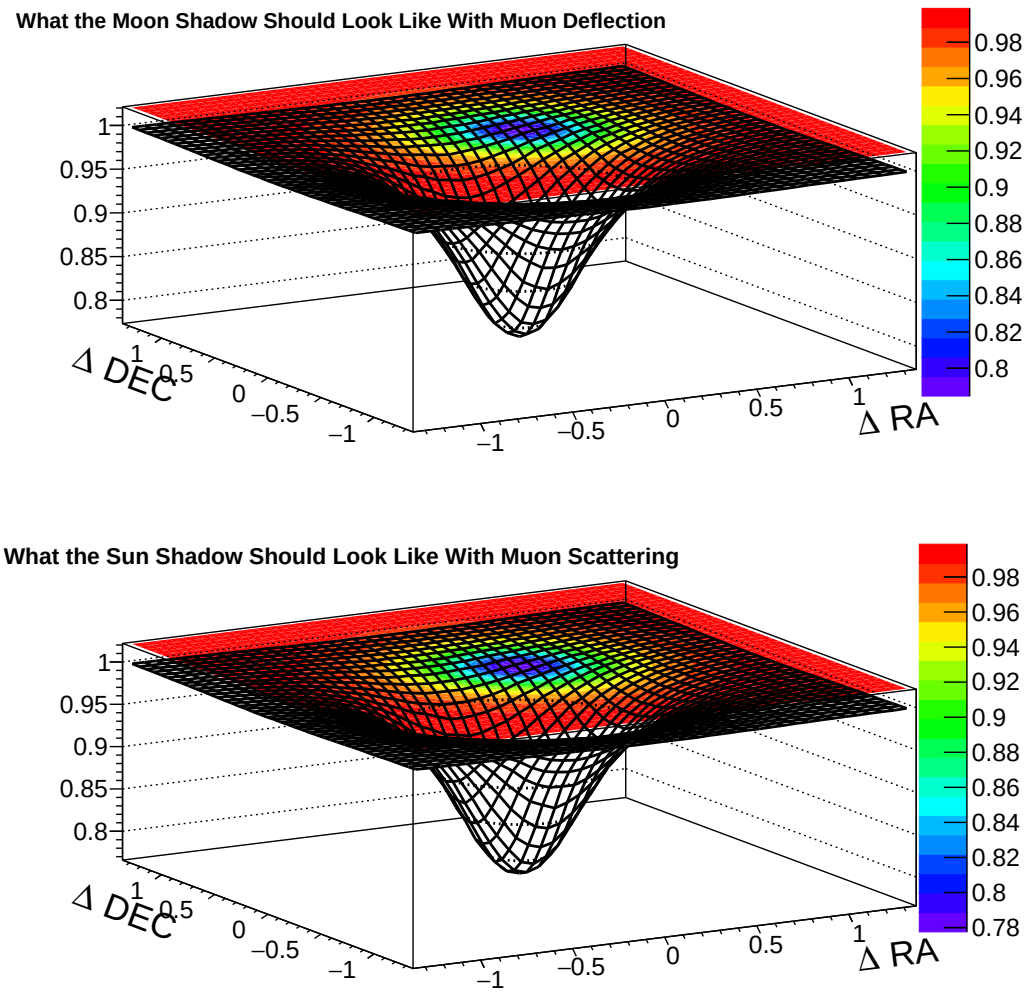

Figure 17: **Histograms representing what the Moon and Sun shadows should look like with cosmic ray muon scattering. Each bin represents the reduction due to the shadowing effect. For example, a bin with 0.8 reduces the number of muons by 20%. Labels are in right ascension and declination, but the histogram would be true for any celestial coordinate system in degrees.**

3.9 Cosmic Ray Muon Background

The Log-Likelihood analysis in Section 4 requires a background. That background must represent what the CR muon data would look like if the Moon and the Sun were not present in the data sample. The background also represents the Null hypothesis of no source present in the data sample, where the 'source' is a cosmic ray 'sink' that absorbs cosmic rays. The methods used to create the Null hypothesis were provided by former UMD graduate student Dan Edie who used them for his Master's thesis.

It is needed to simulate the CR muon data set seen by the FD without any shadowing effects present. In

order to do this, a random position is generated for a muon and a random time at which it occurs. Just randomly sampling muon positions from a histogram of zenith and azimuth will only recreate the data as it was seen by the detector (it would still include shadowing effects). More generally, this simple randomization keeps all the *time dependent* effects such as the Moon and Sun shadows. The Moon and the Sun clearly move in the sky over a day, so including a randomized time will essentially 'mix' up the muons over time (not just over position). For example, imagine that a random position is picked for a muon to have. At this point, it is ambiguous concerning *when* it occurs. It may occur at a time where the Moon is in the same position as the muon, or it may not. If one rolls the dice and picks a random time for this muon as well, then there is a chance that the Moon will have the same position as the muon. Or rather, instead of the "same position", the muon may appear to be within the Moon or Sun radius. If that's the case, then the muon essentially 'fills' up the shadow by just a little bit. Repeat for the whole data set and this effect becomes significant and contributes to the disappearance of the shadowing effects of the Moon and the Sun. This is the principle behind how this background-producing method will provide the Null hypothesis of no shadows present in the data sample.

The first step of this simulation is to pick a random position for a muon. A random zenith and a random azimuth position is pulled out of a 2D histogram of zenith and azimuth (Figure 8). This randomization is done by choosing a random bin and then picking uniformly across that bin to get a value. These two new values can be put into another histogram, as in Figure 18, that shows that this properly simulates the shapes that are expected due to many effects (including but not limited to the geometric and atmospheric effects from Section 3.3.4). It should be noted that this simulation still includes the shadows effects.

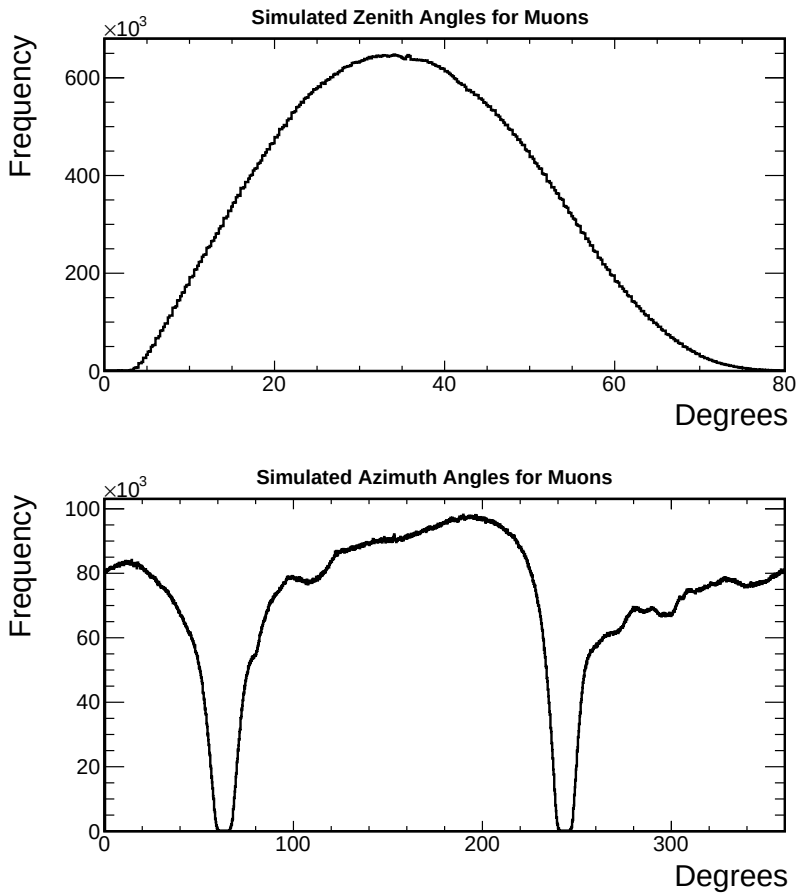

Figure 18: **Simulation of the number of muons seen by the MINOS Far Detector over zenith and azimuth angles from October 2003 and September 2016.**

Next up, a randomized time needs to be found. This step is much more complex than the randomized position step. If the time Δt between each muon occurrence is put into a histogram, this produces Figure 19. An exponential fit is applied to confirm the exponential nature of this distribution. In the second histogram of Figure 19, a log scale is applied which confirms, once again, that this distribution is exponentially decaying. This exponentially decaying nature is expected given the Poisson process that is occurring.

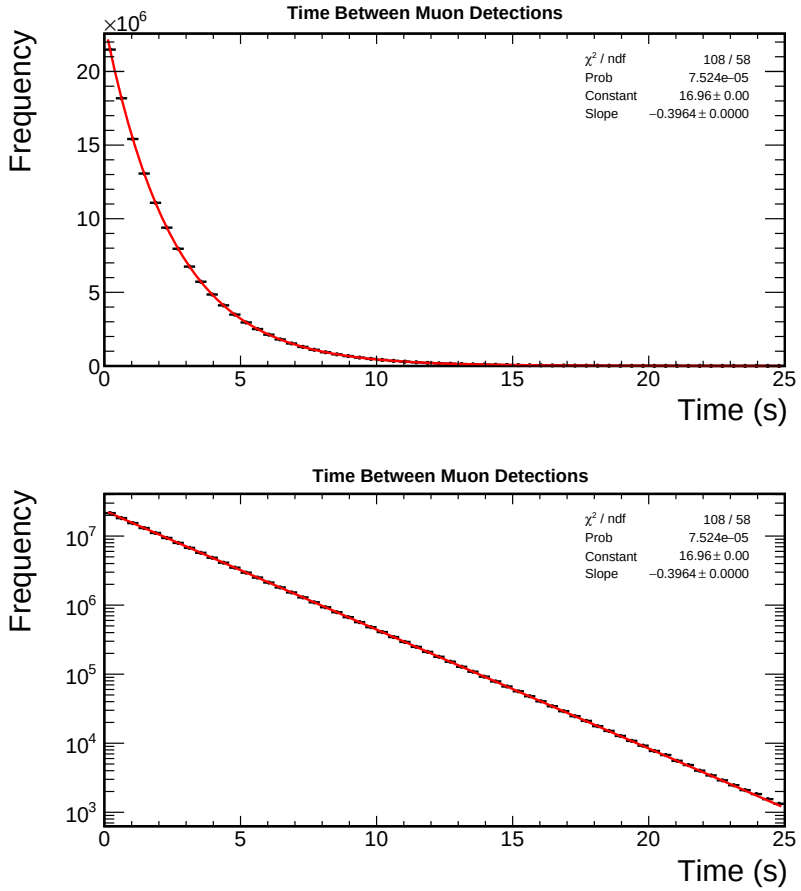

Figure 19: **Time Δt between when muons are detected with an exponential fit (top). On the bottom is the same histogram but with a log scale that reveals a linearity due to the Poisson process.**

Figure 19 must be simulated. To do this, start with a uniform distribution that goes from 0 to 1. It is a flat distribution at 1 for all values of x, where the probability of randomly choosing a value for x is the same for all x. This distribution can be transformed into an exponentially decaying one if the following transformation is applied to each x value

$$t = -ln(x) \tag{22}$$

where "t" is to be the variable for this transformed distribution. Applying this transformation produces an exponentially decaying distribution. This does not yet look exactly like Figure 19. The Fundamental Transformation Law of Probabilities says that under a transformation such as this, the area under the curve with a width dx in the first distribution must equal the area under the curve with a width dt in the transformed distribution [15]. This means that

$$y_x(x)dx = y_t(t)dt \tag{23}$$

where in this problem this becomes

$$(1)dx = e^{-\lambda t}dt \tag{24}$$

$e^{-\lambda t}$ comes from the Poisson process, where λ is the average muon rate during a run of the detector (units of Hz). Rearranging Equation 24 yields

$$1 = e^{-\lambda t}\frac{dt}{dx} \tag{25}$$

where the derivative is

$$\frac{dt}{dx} = \frac{d}{dx}(-ln(x)) = -\frac{1}{x} \tag{26}$$

Thus Equation 25 becomes

$$1 = e^{-\lambda t}|-\frac{1}{x}| \tag{27}$$

where the absolute value is included to avoid negative values in the natural log. Equation 27 can be solved for t to yield

$$t = -ln(x)/\lambda \tag{28}$$

Equation 28 is the transformation that will be used when creating the background. x is a uniform random number in the range from 0 to 1 and t comes out with units of seconds. Carrying out this Monte-Carlo procedure for each muon and applying the transformation in Equation 28 yields Figure 20. This demonstrates that the procedure properly simulates the time between muon occurrences.

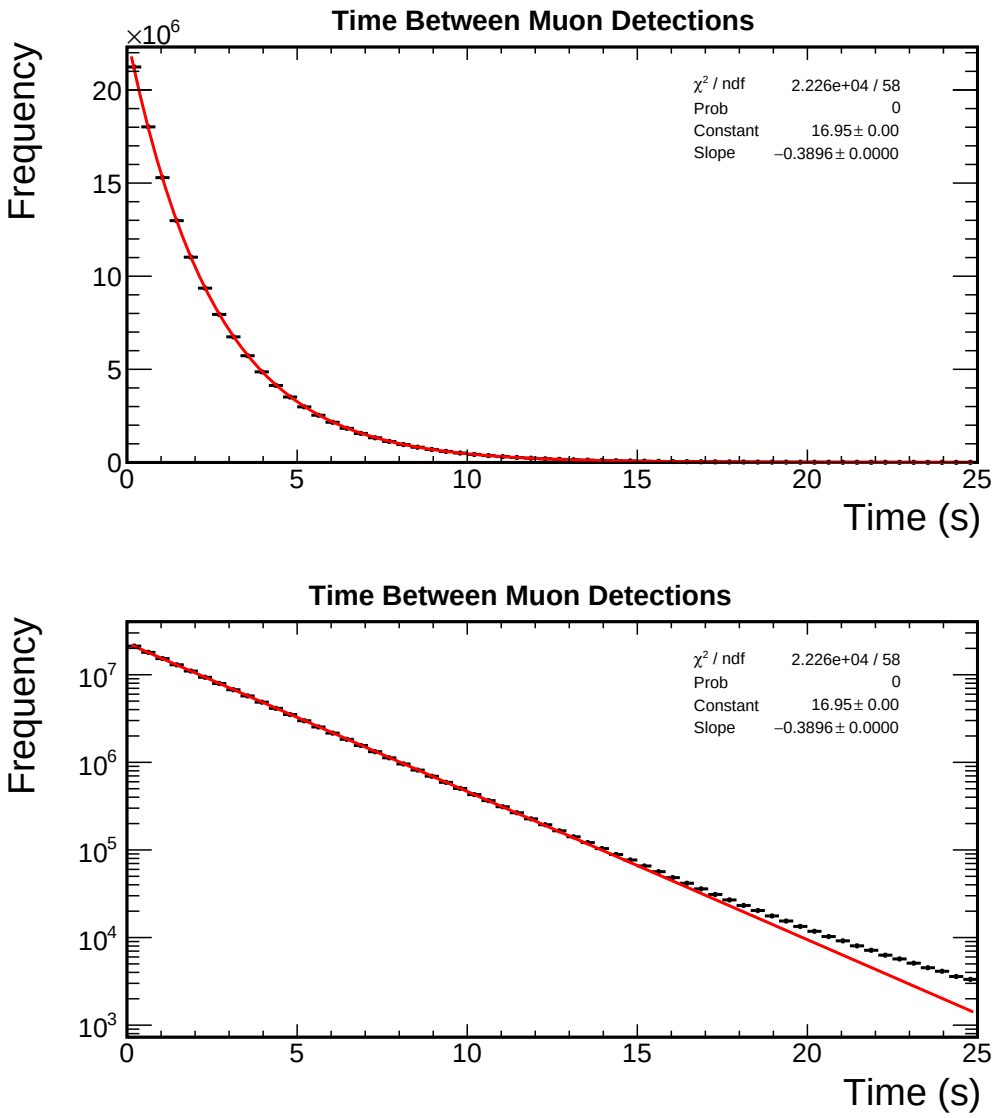

Figure 20: **Simulation of time Δt between when muons are detected with an exponential fit. On the bottom is the same histogram but with a log scale that reveals a linearity due to the Poisson process. At larger times the histogram becomes less linear because the simulation was only ran 3 times (and averaged). Running the simulation more times will produce a more linear histogram at large times, whereas it was run 12 times for the CR shadows in Section 4.**

To simulate Local Sidereal Time and Julian Date, each successive Δt is summed (where consideration is taken for the dates of occurrences). Now a simulated muon position and a simulated time and date for a muon is known. This is expected to remove the shadowing effects from the data sample. In Figure 21, the 1D deficit histograms from Figure 9 are recreated but with the background. These histograms are flat within the Moon and the Sun, which indicates that the shadowing effects have indeed disappeared. To replicate the data with no shadowing effects, there is a randomized position and a randomized time found

for each muon in the data set. The time is used to calculate the Moon and Sun positions to center the histograms at either the Moon or the Sun (like in Figure 10). The positions centered at the Moon/Sun are put into a histogram in right ascension and declination coordinates (Figure 22).

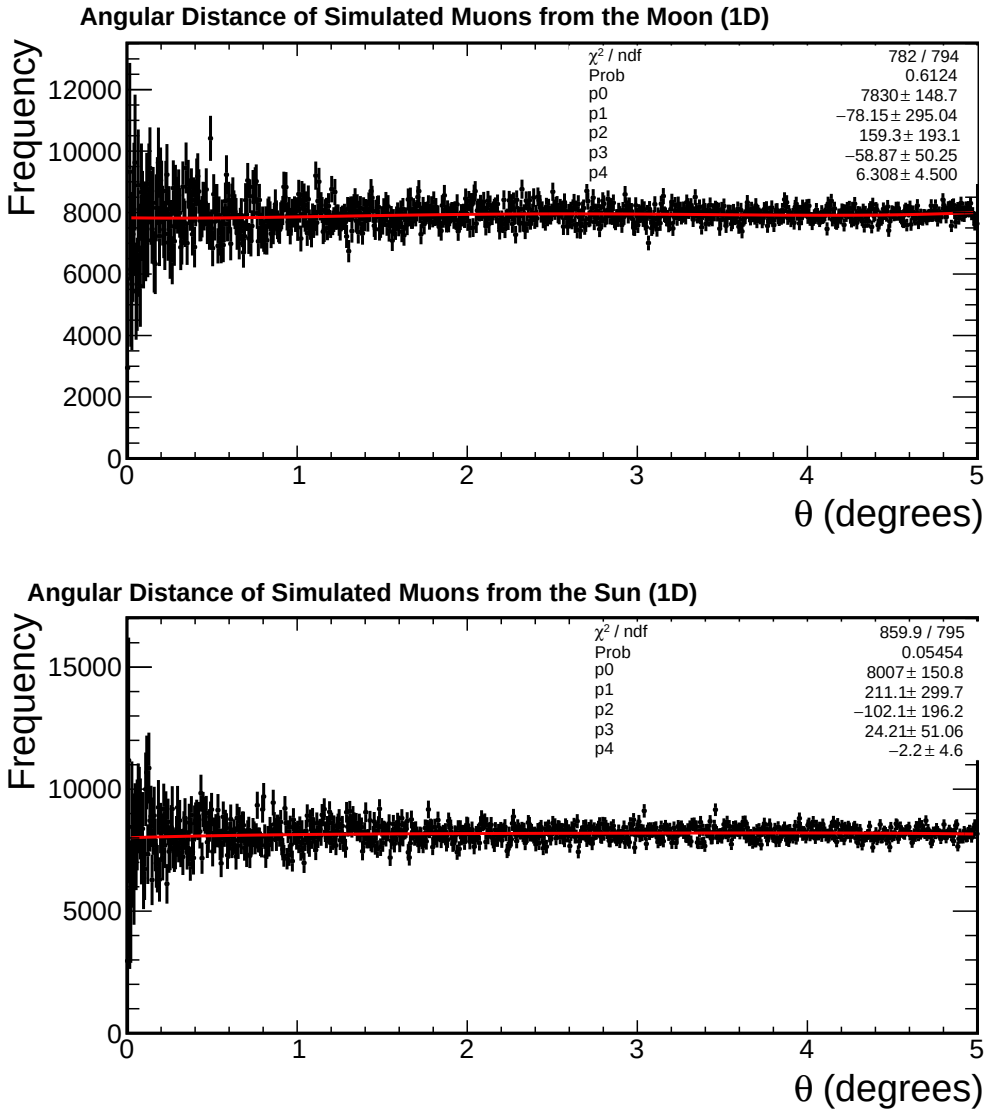

Figure 21: **1D muon deficits in the regions around the Moon and the Sun without shadowing effects. The simulation was done for the whole data set 3 times and averaged.**

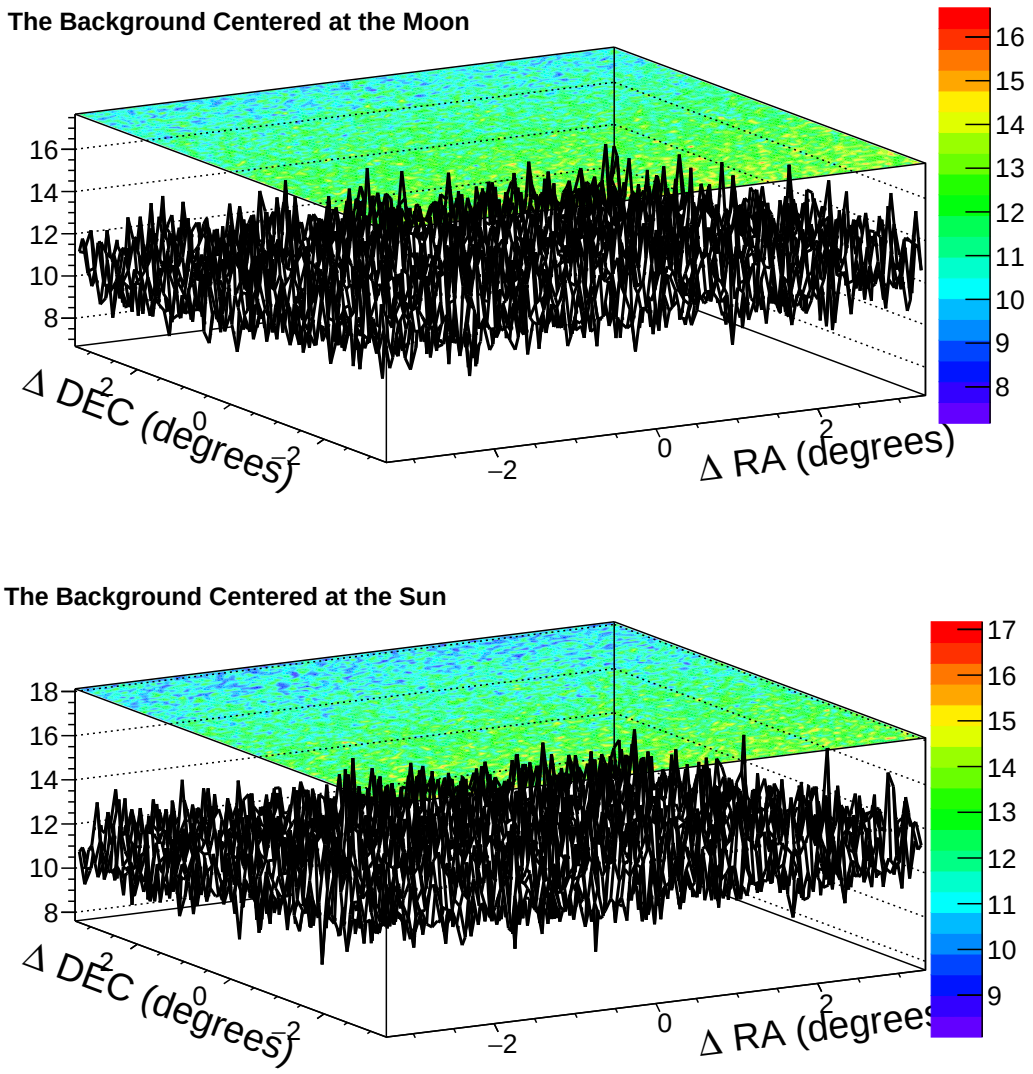

Figure 22: **Null hypothesis of no shadowing effects present for the Moon (left) and the Sun (right). Center of the histograms represent the center of the Moon/Sun. The number of muons slightly increases over declination because of the zenith angle dependence of the cosmic ray muon flux.**

The background thus constitutes a good Null hypothesis of no shadowing effects present, though other acceptance effects are accounted for too.

4 Log-Likelihood Analysis and Cosmic Ray Shadows

Now everything is made that is required to create CR shadows: The signal histogram (Figure 10), the shadow template (Figure 17), and the Null hypothesis (Figure 22). The Log-Likelihood analysis is a binned analysis that utilizes

$$\lambda(S_i) = 2\sum_{i=1}^{n_{bin}}[N_i^{th} - N_i^{obs} + N_i^{obs} ln(N_i^{obs}/N_i^{th})] \tag{29}$$

where i is the bins of the template, N_i^{obs} is the observed muon counts at bin i, and $N_i^{th} = N_i^{back} * S_i$ where S_i is the value in the template at bin i and N_i^{back} is the expected counts given no shadowing effects. N_i^{th} is the expected counts in the presence of a cosmic ray sink. The summation is done over all the bins of the template. Figure 23 demonstrates this analysis. The red (smallest) histogram is the Moon/Sun template that slides around the blue (biggest) signal and background histograms to fill in the orange histogram. At each location, a summation over all the template bins and respective signal and background bins is evaluated to get a value at each orange bin. The value represents the log-likelihood that the Moon/Sun templates centered at each location matches the data better than the Null hypothesis of no shadow at all.

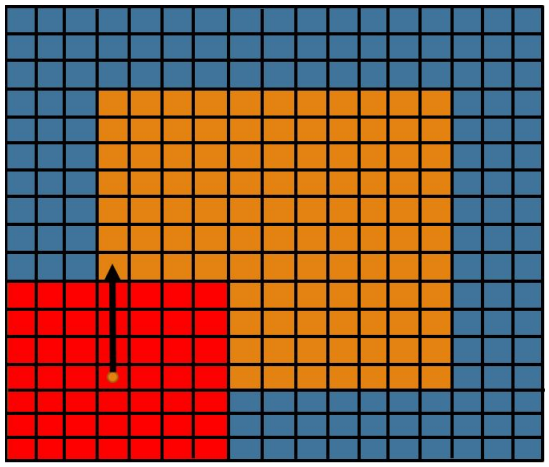

Figure 23: **Cartoon that demonstrates the Log-Likelihood analysis. Red (smallest) is the shadow template, blue (biggest) is the signal and background histograms, and the orange is the Log-Likelihood histogram. The Log-Likelihood is calculated for the bin with the dot: *i.e.*, how well does a shadow centered at that point match the data?**

To determine the strength of the shadowing effect, the following parameter is defined:

$$\Lambda = \lambda(0) - \lambda(S_i) \tag{30}$$

$\lambda(S_i)$ is λ evaluated with the reduction determined by the template and $\lambda(0)$ is λ evaluated with no re-

duction at all (no shadowing effects present). $\lambda(S_i)$ measures how well the data in a region is described by a shadow. The larger $\lambda(S_i)$ is, the better the data is described by a shadow. $\lambda(0)$ measures how well the data in a region is described by no shadow at all. The larger $\lambda(0)$ is, the better the data is described by the Null hypothesis. This means that a large positive value for Λ indicates the likely presence of a shadowing effect, but negative values indicate only the presence of background. The calculated Moon and Sun shadows are shown in Figure 24 (negative values omitted).

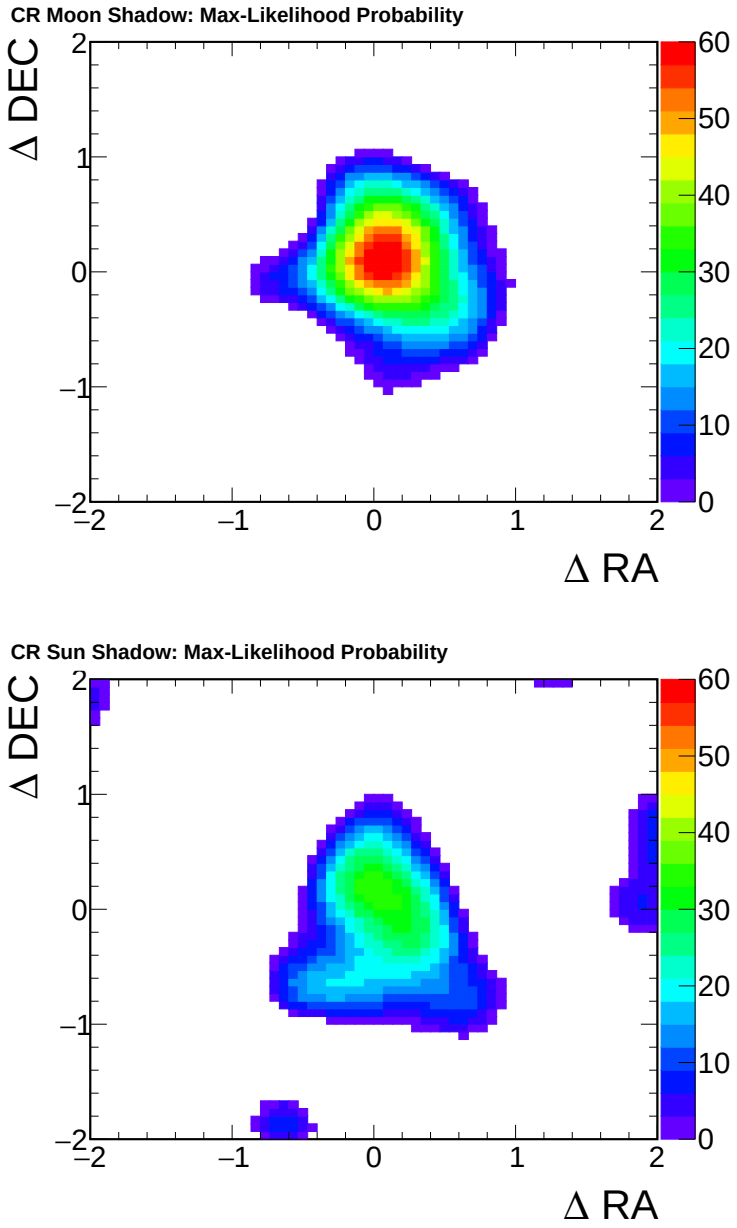

Figure 24: **Moon and Sun shadows seen by the MINOS Far Detector from 2003-08 to 2016-07. Bin size is** $0.066°$**. These omit the negative values on the histogram scale which represent regions best described by the Null hypothesis. Notice that the Sun shadow appears smeared out, as a result of heliospheric magnetic field influence, while the Moon shadow does not.**

The Sun shadow appears much less significant than the Moon shadow and more smeared out. This is likely a result of the heliospheric magnetic field that greatly influences the trajectories of CRs. The Moon shadow seems largely unaffected by the heliospheric magnetic field, which confirms the suspicion that the Moon is close enough for CRs to be deflected little by it. The Sun shadow appears weaker (with smaller values of Λ) potentially because the Sun shadow is smeared and also wobbles around so much over the 13 years.

The Moon shadow stays in the same position which keeps making the effect stronger overall. The Moon shadow stayed consistent over the 13 years as evidenced by its circular-like shape and large Λ values.

5 Conclusions

Many things were explored and demonstrated in this research. The cosmic ray shadows were found for the Moon and the Sun using 141 million muons observed by the MINOS Far Detector. The Sun shadow varied over time and was smeared out and less significant than the Moon shadow, whereas the Moon shadow stayed put and was much clearer and significant overall. This confirmed the expectation that the Moon shadow would not be affected much by the heliospheric magnetic field. The expectation that the Sun shadow would be affected significantly by the heliospheric magnetic field was confirmed. Next up is to investigate how the heliospheric magnetic field affects the cosmic ray shadows over time. That analysis would be easier using the MINOS Near Detector which has a much larger data set of cosmic ray muons available for analysis. Another avenue of research is to investigate the effect of the geomagnetic field on cosmic rays using cosmic ray shadows. That analysis, once again, would be much easier with the MINOS Near Detector as a result of the high cosmic ray muon flux and higher elevation. The exploration of the cosmic ray muon scattering phenomenon revealed that cosmic ray muon deflection can be simulated using binomial statistics and Monte-Carlo methods. It was revealed that there is still much more to explore with regards to cosmic ray muon deflection.

References

[1] Todor Stanev. *High energy cosmic rays; 2nd ed.* Praxis Publishing, Chichester, 2010.

[2] Thomas K Gaisser, Ralph Engel, and Elisa Resconi. *Cosmic rays and particle physics; 2nd ed.* Cambridge University Press, Cambridge, 2016.

[3] P. Adamson et. al. Observation in the minos far detector of the shadowing of cosmic rays by the sun and moon. *Astroparticle Physics*, 34(6):457 – 466, 2011.

[4] M. Amenomori et. al. Cosmic-ray deficit from the directions of the moon and the sun detected with the tibet air-shower array. *Phys. Rev. D*, 47:2675–2681, Apr 1993.

[5] F. Bos, F. Tenholt, J. Becker Tjus, and S. Westerhoff. Observation of the cosmic-ray shadow of the moon and sun with icecube. *ASTRA Proceedings*, 2:5–8, 2015.

[6] M. Ambrosio et. al. Moon and sun shadowing effect in the macro detector. *Astroparticle Physics*, 20(2):145 – 156, 2003.

[7] O. C. Allkofer and P. K. F. Grieder. *Cosmic rays on earth.* 1984.

[8] M. Amenomori et al. Moon shadow by cosmic rays under the influence of geomagnetic field and search for antiprotons at multi-tev energies. *Astroparticle Physics*, 28(1):137 – 142, 2007.

[9] M. Amenomori et. al. Probe of the solar magnetic field using the "cosmic-ray shadow" of the sun. *Phys. Rev. Lett.*, 111:011101, Jul 2013.

[10] Juan Pedro Ochoa Ricoux. *The MINOS Experiment*, pages 39–66. Springer New York, New York, NY, 2011.

[11] D.G. Michael et al. The magnetized steel and scintillator calorimeters of the minos experiment. *Nuclear Instruments and Methods in Physics Research Section A: Accelerators, Spectrometers, Detectors and Associated Equipment*, 596(2):190 – 228, 2008.

[12] Juan Pedro Ochoa Ricoux. *A Search for Muon Neutrino to Electron Neutrino Oscillations in the MINOS Experiment.* PhD thesis, California Institute of Technology, Jan 2010.

[13] Peter Duffett-Smith. *Practical astronomy with your calculator; 3rd ed.* Cambridge University Press, Cambridge, 1989.

[14] Rene Brun and Fons Rademakers. Root - an object oriented data analysis framework. *Proceedings AIHENP'96 Workshop, Lausanne, Nucl. Inst. and Meth. in Phys. Res. A 389 (1997) 81-86.*, Sep. 1996.

[15] Brian P Flannery, William H Press, Saul A Teukolsky, and William Vetterling. Numerical recipes in c. *Press Syndicate of the University of Cambridge, New York*, 24:78, 1992.